International Journal of Polymer Science

Sustainable Bio-based Nanofiller Polymer Composites

Lead Guest Editor: Vijaya Kumar Rangari
Guest Editors: Deepa Kodali, Derval Dos Santos Rosa, and Maria L. Auad

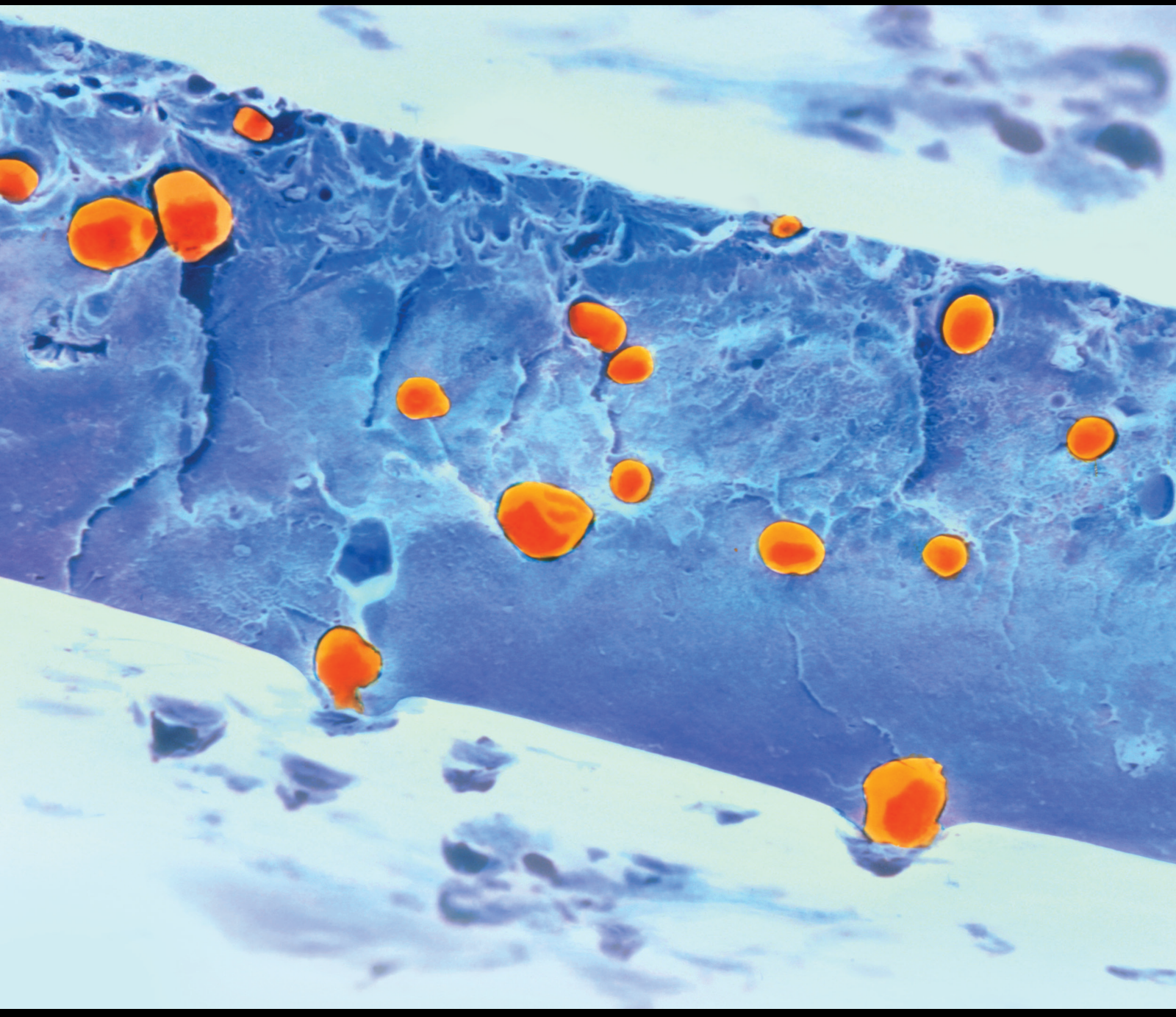

Sustainable Bio-based Nanofiller Polymer Composites

International Journal of Polymer Science

Sustainable Bio-based Nanofiller Polymer Composites

Lead Guest Editor: Vijaya Kumar Rangari
Guest Editors: Deepa Kodali, Derval Dos Santos Rosa, and Maria L. Auad

Contents

Hindawi
International Journal of Polymer Science
Volume 2022, Article ID 6762449, 13 pages
https://doi.org/10.1155/2022/6762449

Research Article

Cracking Behaviour of Alkali-Activated Aluminosilicate Beams Reinforced with Glass and Basalt Fibre-Reinforced Polymer Bars under Cyclic Load

S. Nagajothi,[1] **S. Elavenil**,[1] **S. Angalaeswari**,[2] **L. Natrayan**,[3] **and Prabhu Paramasivam**[4]

[1]*School of Civil Engineering, Vellore Institute Technology, Chennai, Tamil Nadu, India*
[2]*School of Electrical Engineering, Vellore Institute Technology, Chennai, Tamil Nadu, India*
[3]*Department of Mechanical Engineering, Saveetha School of Engineering-SIMATS, Chennai, Tamil Nadu, India*
[4]*Department of Mechanical Engineering, College of Engineering and Technology, Mettu University, Metu - 318, Ethiopia*

Correspondence should be addressed to S. Nagajothi; naga.jothis2014phd1138@vit.ac.in, S. Elavenil; elavenil.s@vit.ac.in, S. Angalaeswari; angalaeswari.s@vit.ac.in, L. Natrayan; natrayanphd@gmail.com, and Prabhu Paramasivam; prabhuparamasivam21@gmail.com

Received 27 November 2021; Revised 24 June 2022; Accepted 17 August 2022; Published 13 September 2022

Academic Editor: Qinglin Wu

Cement is an essential material for concrete, which is mostly used worldwide second to the consumption of water. Due to the emission of CO_2 into the atmosphere, the alternative material of geopolymer concrete was used. In this research work, silica and alumina content such as ground granulated blast furnace slag (GGBS), fly ash, and triggered by alkali activator solutions were used in geopolymer concrete. Due to the dwindling of river sand, alternative material of manufactured sand (M-Sand) was considered. To avoid corrosion problems in reinforced concrete structures, glass fibre reinforced polymer (GFRP) and basalt fibre-reinforced polymer (BFRP) bars were used as an alternative material for steel reinforcement in this work. As per the code, IS: 10262, the concrete mix design of M30 grade has arrived for the control mix and the same proportion was adopted for geopolymer concrete. Six beams of geopolymer and a concrete control beam of $100 \times 160 \times 1700$ mm were cast and examined under a four-point cyclic load. Cyclic load results were compared with static load under ambient curing. Residual deflection, moment capacity, energy dissipation, and stress–strain behaviour results were compared and discussed. A sudden shear and premature failure were observed in FRP beams under static and cyclic bending tests.

1. Introduction

The emission of greenhouse gases mainly causes an environmental impact on the atmosphere and impacts climate change. Many countries are entrusted with reducing the global carbon footprint issue, which makes climate change mainly caused by the cement production (expected to reach 550 million tonnes by 2020 as per the cement manufacturers association) in industries. The alternative material for cement is clinker-free binders such as geopolymer produced from the reaction between precursors of aluminosilicate materials and alkaline activator solution [1]. These alkali-activated materials show good mechanical properties, which include fire and acid resistance [2], thermal resistance [3] and durability properties [4] with less carbon dioxide emission and energy costs. The researchers reported that the by-product of ground granulated blast furnace slag (GGBS) and fly ash (FA) is the most preferred materials for producing geopolymer material using alkali activator solutions [5]. Ghina et al. used FA, GGBS, and silica fume in geopolymer concrete under ambient curing conditions and evaluated the mechanical properties, microstructural, and environmental impact. The authors inferred that the footprints of carbon emissions were decreased by more than 60% [6]. The flooding was caused due to the depletion of natural sand in quarrying activities and the urgent need to use a replacement material for concrete making. Manufactured sand (M-sand) from the waste of crushed granite aggregates has not shown any adverse effect on strength properties when replacing

natural sand [7]. Traditional steel bars do not have corrosion resistance properties; it causes damage to the existing concrete structures in an aggressive environment [8]. To reduce the corrosion problem in steel bars, many techniques like an epoxy coating, galvanizing, decreasing permeability, waterproofing of concrete, etc., have been tried [9]. But none of the methods had properly solved the corrosion problem. The use of fibre-reinforced polymer (FRP) bars is an emerging technology in concrete structures instead of steel bars to resist corrosion. The FRP bars have the advantage of high corrosive resistance, easy handling, and non-conductivity properties over steel bars [10]. Glass, carbon, aramid, and basalt FRP bars are commonly used in the civil engineering sector.

Kalpana and Subramanian have discussed the load-deflection, crack pattern and crack width using GFRP bars and steel bars in conventional concrete by varying the grade of concrete and concluded that GFRP bars reinforced beams in high-strength concrete showed better results compared with other bar reinforcement beams [11]. Osama Ahmed et al. studied the effect of stiffness, and flexural strength of BFRP reinforced concrete beams by varying the parameter like reinforcement ratio and revealed that an increase in reinforcement ratio improved the beam's ultimate load-carrying capacity and stiffness [12]. Nagajothi and Elavenil reported the strength of geopolymer concrete by varying M-sand percentage under the heat curing process [13]. Zike et al. investigated durability using seawater and sea sand concrete along with BFRP and GFRP bars to avoid a shortage of resource material and corrosion problems [14]. Researchers used GFRP bars in geopolymer concrete externally wrapped in columns for an effective retrofitting technique [15]. Sarker concluded that the geopolymer concrete bond strength was higher than the ordinary Portland cement concrete for the same parameter [16].

Many researchers studied the microstructural characterization and durability studies on geopolymer concrete, flexural behaviour of steel in conventional and geopolymer concrete, and flexural behaviour of FRP bars in conventional concrete. The lack of studies available on FRP bars in geopolymer concrete using manufactured sand induces to take this research. In this study, the geopolymer concrete beams flexural behaviour using GFRP and BFRP bars reinforcement under a four-point cyclic load test were carried out and the results of load-deflection behaviour, moment–curvature relation, stress–strain, crack spacing, crack propagation, average crack width, and several cracks were noted, and crack pattern was also discussed and compared with beams under static load.

2. Materials and Methods

2.1. Reinforcing Bars. The FRP bars of GFRP and BFRP bars for 12 mm and 10 mm diameter rods were used as main reinforcement bars and 8 mm diameter bars for shear reinforcement in geopolymer concrete and 12 mm and 10 mm diameter steel rods in control concrete. The properties of modulus elasticity, Poisson's ratio, and tensile strength for BFRP, GFRP, and steel rods are given in Table 1. Different sizes of GFRP and BFRP bars are presented in Figure 1.

Table 1: Properties of reinforcement bars.

Properties	BFRP	GFRP	Steel
Elastic modulus (GPa)	94	54	200
Poisson's ratio	0.23	0.24	0.27
Tensile strength (MPa)	513	495	515

2.2. Stirrups Used in Reinforcing Bars. The 8 mm diameter steel bars were used as stirrups in control concrete. At the same time, the 8 mm diameter BFRP and GFRP bars were used as stirrups in geopolymer concrete. As FRP bars are brittle, it is very difficult to bend FRP rods for stirrups. Hence the stirrups of FRP (GFRP and BFRP) rod were prepared by an amalgamation of vertical and horizontal bars using epoxy resin, and the joint was externally wrapped with FRP mats (GFRP and BFRP mats).

2.3. Ingredients for Concrete. The ingredients used for making geopolymer concrete are FA, GGBS, M-sand, coarse aggregate (20 mm, 12 mm, 8 mm), alkali activator solutions, and superplasticizer. FA and GGBS with a specific gravity of 2.13 and 2.85 correspondingly were used in geopolymer concrete obtained from the thermal power plant and Astra Chemicals, Chennai. The specific gravity of river sand, M-sand, and coarse aggregates are the same as those of 2.66, 2.72, and 2.73. The aggregates used for making geopolymer concrete were in the Saturated Surface Dry (SSD) condition.

3. Specimen Design, Details, and Preparation

3.1. Specimen Design. Based on mix designs and trail mixes, the adopted quantity of materials for geopolymer and control concrete are given in Table 2. The ratio of alkaline activator solution to binder was 0.45 and 2.5 for Na_2SiO_3 to NaOH ratio. Conplast SP430 was taken as 1% of the binder to attain the desired workability in geopolymer concrete.

The geopolymer and control concrete test specimens were cast and tested according to the mix quantities. A cube size of 150 mm × 150 mm × 150 mm was used to calculate the compressive strength. The modulus of elasticity, the compressive strength of geopolymer, and control concrete are 19.10 GPa, 40.35 MPa, and 22.19 GPa, 38.95 MPa, respectively. The strength properties were validated by developing the Levenberg–Marquardt algorithm using MATLAB software [17].

3.2. Specimen Details. The size of beam specimens for a width of 100 mm, depth of 160 mm, and length of 1700 mm were taken [18]. Six reinforced beam specimens were cast and tested under static and cyclic load conditions. The geometry and reinforcement details of the beam are shown in Figure 2.

Among the six beams, two were reinforced with BFRP bars with BFRP stirrups in geopolymer concrete, two were reinforced with GFRP bars with GFRP stirrups in geopolymer concrete, and the remaining two were reinforced with steel bars with steel stirrups in control concrete. In all six beams, two numbers of 12 mm diameter rods were

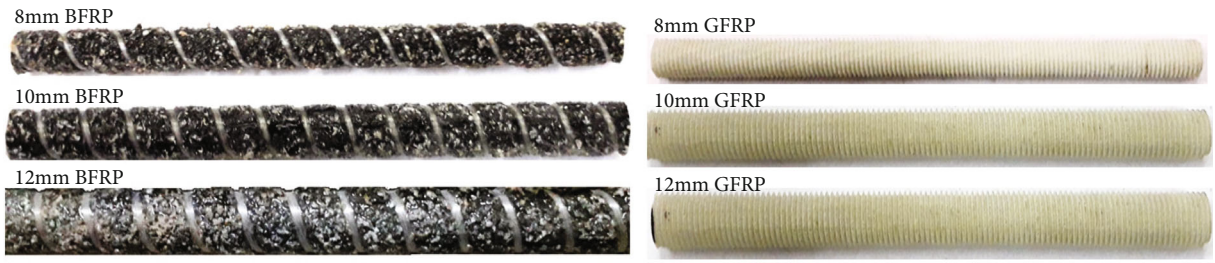

Figure 1: Different sizes of BFRP and GFRP bars.

Table 2: Quantity of materials adopted for geopolymer and control concrete.

Geopolymer concrete (kg/m^3)		Control concrete (kg/m^3)	
Materials	Quantity	Materials	Quantity
Fly ash	304	Cement	380
GGBS	76		
M-sand	660	River sand	660
Coarse aggregate	1189	Coarse aggregate	1189
AAS	171	Water	171
Superplasticizer	3.8		

Note: M-sand-Manufactured sand, AAS-Alkaline Activator Solutions.

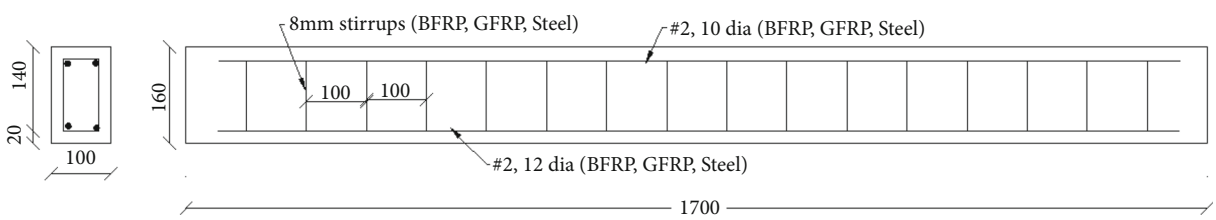

Figure 2: Geometry and reinforcement details of the beam (all dimensions are in mm).

positioned in the tension zone, two numbers of 10 mm diameter rods were positioned in the compression zone, and 8 mm stirrups rods spacing of 100 mm C/C [19]. The beams were designated as A–B–C. A denotes the bars like basalt, glass, and steel, B denotes the concrete type like geopolymer and control, and C denotes cyclic or static loading conditions. For example, BRGC-C denotes basalt reinforced geopolymer concrete under cyclic load, and BRGC-S denotes basalt reinforced geopolymer concrete under static load. The longitudinal reinforcement ratio adopted for all the beams is 2.4%.

3.3. Specimen Preparation. The aggregates (SSD condition) were mixed with the binders and an alkaline activator solution was poured into the mixer machine. Mixing was sustained for 5 minutes [20]; after that superplasticizer was added to this mix to attain the workability of concrete. The geopolymer concrete in a new state was placed in the beam mould in three equal layers and compacted by a vibrator. After 24 hours, the beam was demoulded and kept at ambient temperature for geopolymer concrete and water curing for control concrete is 28 days [21]. After the curing period, the beam was tested for finding the flexural behaviour of geopolymer concrete for the cyclic and static load. The BFRP and GFRP bars cages are shown in Figure 3(a) and 3(b).

3.4. Test Setup and Procedure. Four-point static and cyclic bending tests were employed to examine the flexural behaviour of geopolymer concrete beams reinforced with BFRP, GFRP, and control concrete beams reinforced with steel. The beams were reared on a steel box girder of length 1700 mm and the effective span of the beam was 1500 mm. The beam was loaded at four points, each 250 mm away from the center to the load point. During the specimen test, the 1000 kN capacity of the universal testing machine (UTM) was used [22]. The schematic and test setup for the flexural test under the cyclic test are shown in Figures 4.

3.5. Test Setup for Cyclic Load. FRP reinforced geopolymer concrete beams and steel-reinforced control concrete beams were tested to the ultimate load level under static and cyclic load. The load increment chosen was 3 kN and 5 kN for FRP reinforced beams and steel-reinforced beams, respectively, which was applied gradually to reach peak cyclic load of 6 kN, 9 kN, 12 kN, 15 kN, and 18 kN in each cycle for FRP beams and 10 kN, 15 kN, 20 kN, and 25 kN in each cycle

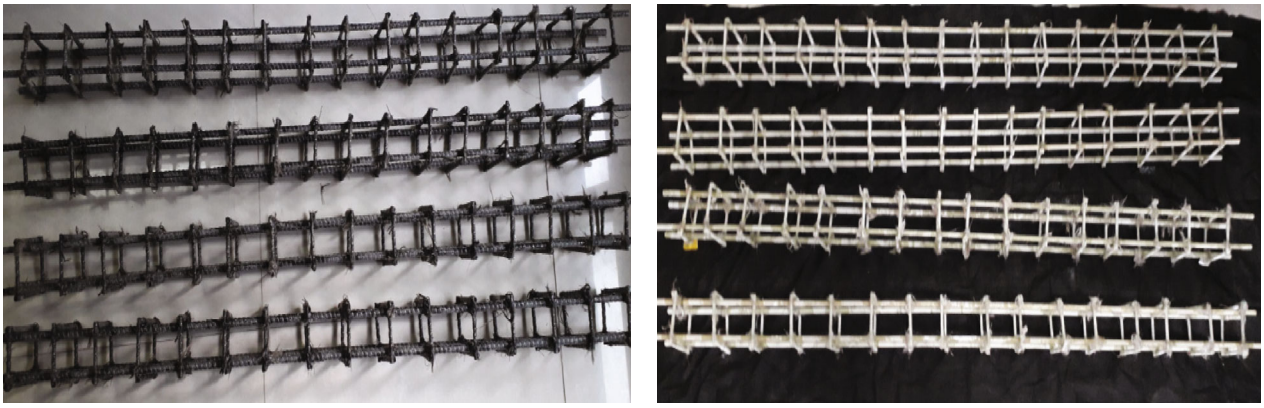

(a) (b)

Figure 3: (a) BFRP reinforcement cages. (b) GFRP reinforcement cages.

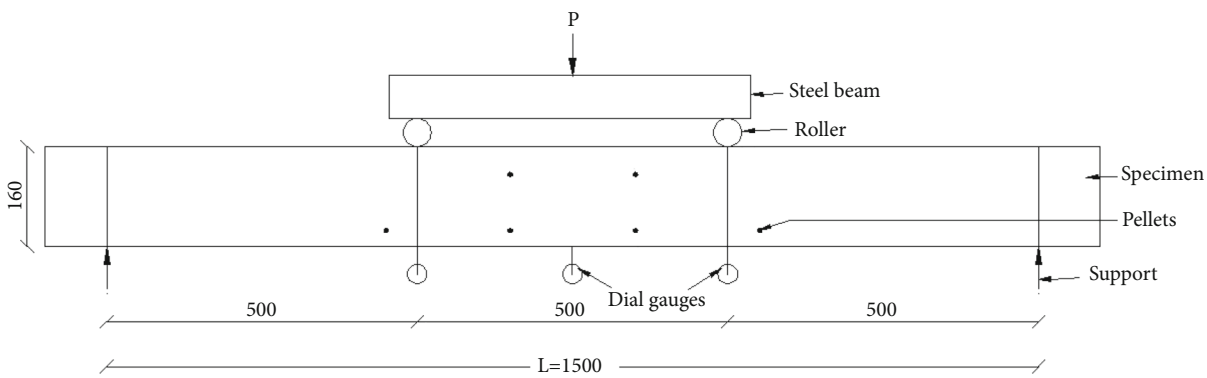

(a)

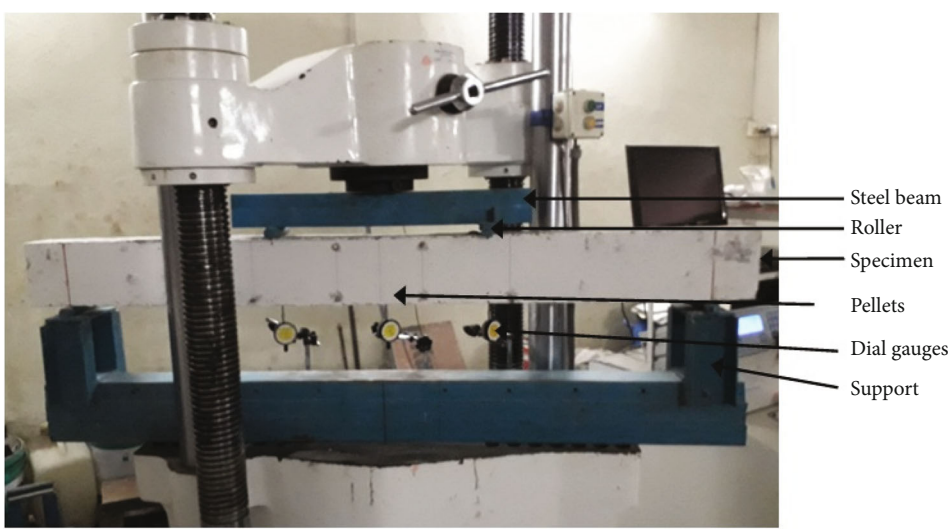

(b)

Figure 4: (a) Test setup of the beam for the cyclic load (all dimensions are in mm). (b) Flexural test setup and instrumentation.

for steel beams [23]. The specimen was loaded up to 18 kN and 25 kN for FRP and steel beams and the load was released in reverse order to reach 0 kN. This is considered one cycle and continues till the 5th cycle. After the 5th cycle, the load increased gradually like 3 kN and 5 kN for FRP and steel beams to reach the ultimate load level. At each load interval, residual deflection, moment capacity, energy dissipation, and stress–strain behaviour were also observed for all the beams examined under cyclic load. Compared with beams examined under static load conditions [24]. Mode

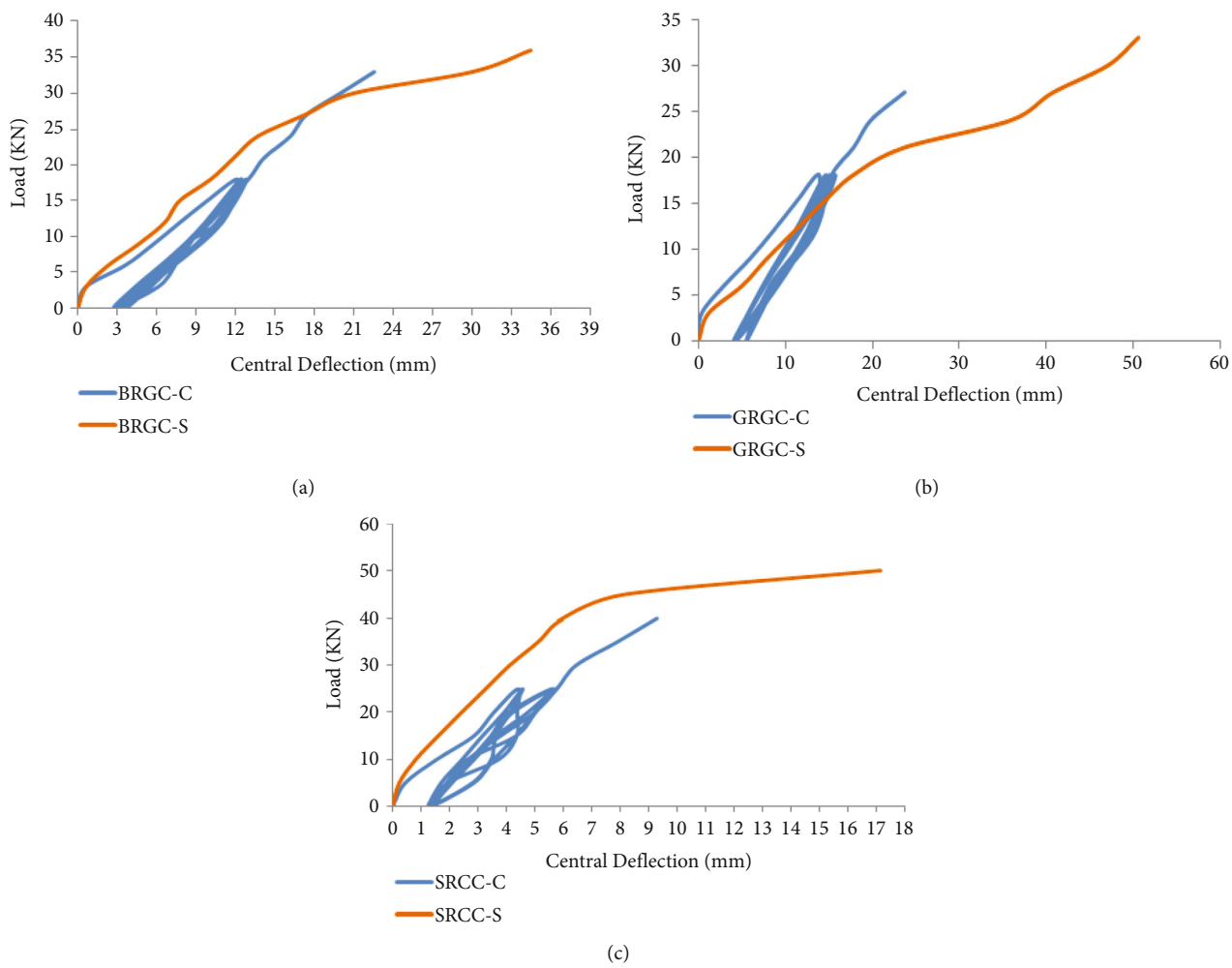

Figure 5: (a) Load-central deflection of BRGC beams, (b) load-central deflection of GRGC beams, and (c) load-central deflection of SRCC beams.

of failure and crack behaviour for the first crack load and ultimate load level of the beams was also observed.

4. Experimental Results and Observations

4.1. Load-Deflection Behaviour. Load-central deflection behaviour of FRP and steel rods reinforced beams under cyclic loads are plotted compared with static loading conditions. Load-central deflection of BRGC, GRGC, and SRCC beams under cyclic and static loads are shown in Figures 5(a), 5(b), and 5(c), respectively. The load-carrying capacity of all the beams under static load increases compared with cyclic load [25]. Under cyclic load, the deflection of GRGC and BRGC beams in geopolymer concrete is higher than SRCC beams in control concrete. The patterns of load-deflection of FRP beams in geopolymer concrete are similar to the steel bars in control concrete beams. The stiffness values for all the beams under cyclic and static load are given in Table 3.

From Table 3, it is observed that the stiffness is reduced under cyclic load for all the beams compared with the static load. There is a sudden increase in deflection due to stiffness reduction of beams after placing a particular load of 30 kN, 21 kN, and 21 kN for BRGC, GRGC, and SRCC, respectively. The percentage reduction and increase of stiffness in BRGC-C, SRCC-C, and GRGC-C beams are 13.9%, 47.8%, and −27.5%, respectively, under cyclic load compared with the static load.

The residual deflection for BRGC-C, GRGC-C, and SRCC-C beams under cyclic load is given in Table 4. The energy dissipation for BRGC-C, GRGC-C, and SRCC-C beams under cyclic load is given in Table 5.

From Table 4, it is inferred that the residual deflection values are higher in FRP rods in geopolymer concrete compared with steel rods in control concrete. The increase in residual deflection for BRGC-C, GRGC-C, and SRCC-C beams is 32%, 30%, and 10%, respectively, from cycle 1 to cycle 5.

From Table 5, it is observed that the energy values for GRGC are higher than BRGC in geopolymer concrete and SRCC in control concrete due to its brittle nature. At the end of the 5th cycle, the energy values are reduced compared with initial energy dissipation values in all the beams. The reduction in energy dissipation percentages is 87.60%, 80%,

Table 3: Stiffness of beams under cyclic and static loads.

Materials	BRGC	GRGC	SRCC
Stiffness-cyclic load (kN/mm)	1.55	1.39	6.45
Stiffness-static load (kN/mm)	1.80	1.49	12.35

Table 4: Residual deflection of BRGC-C, GRGC-C, and SRCC-C under cyclic loads.

Cycles/ materials	BRGC-C (mm)	GRGC-C (mm)	SRCC-C (mm)
Cycle 1	2.79	3.95	1.25
Cycle 2	2.81	4.07	1.26
Cycle 3	3.20	4.16	1.31
Cycle 4	3.46	4.54	1.32
Cycle 5	3.68	5.51	1.37

Table 5: Energy Dissipation of BRGC-C, GRGC-C, and SRCC-C under cyclic loads.

Cycles/ materials	BRGC-C (kN mm)	GRGC-C (kN mm)	SRCC-C (kN mm)
Cycle 1	56.88	81.68	33.83
Cycle 2	16.95	26.08	15.68
Cycle 3	10.1	19.1	13.89
Cycle 4	9.79	19.1	11.83
Cycle 5	7.03	16.44	11.22

and 66.83% for BRGC-C, GRGC-C, and SRCC-C under cyclic load from cycle 1 to cycle 5. The reduction of energy dissipation in FRP beams in geopolymer concrete is higher than in steel bars in control concrete.

4.2. Moment–Curvature Relationship. The moment–curvature relationship of FRP and steel bars under cyclic and static load are shown in Figures 6(a), 6(b), and 6(c), respectively. Using the area moment theorem from equation (1), the curvature was calculated using measured deflections.

$$\varnothing d = \frac{8\partial}{l^2}, \qquad \partial = \mathrm{D}_2 - \frac{\mathrm{D}_1 + \mathrm{D}_3}{2}, \tag{1}$$

where $\varnothing d$ is the deflection curvature, l is distance between load points, D_1 and D_3 are the load point deflection, and sD_2 is the central deflection.

Figures 6(a), 6(b), and 6(c) show that the moment–curvature relationship of BRGC and GRGC is similar in both cyclic and static loading conditions. The curvature value is almost the same under cyclic and static loading conditions. Also, the value of moment–curvature is smaller in cyclic load than the static load. In SRCC, the moment–curvature relationship pattern is different than FRP rods in geopolymer concrete.

4.3. Flexural Stress-Compressive and Tensile Strain Behaviour of Beams. The behaviour of flexural stress-compressive and tensile strain for BRGC, GRGC, and SRCC beams under cyclic and static load are shown in Figures 7(a), 7(b), and 7(c), respectively. The maximum tensile strain in all the beams is slightly higher in static than cyclic load. The maximum compressive strain in all the beams under cyclic and static loads is almost equal. The residual compressive and tensile strain values for BRGC-C, GRGC-C, and SRCC-C under cyclic load are given in Table 6.

From Table 6, it is observed that the residual compressive and tensile strain values show a slight increase from cycle 1 to cycle 5 under cyclic load conditions for all the beams. The residual compressive strain for BRGC-C and GRGC-C is increased around 6 times from cycle 1 to cycle 5. But in SRCC-C, it increases 3.8 times from cycle 1 to cycle 5. The residual tensile strain for BRGC-C, GRGC-C, and SRCC-C increased 4.7 times, 1.5 times, and 1.7 times, respectively, from cycle 1 to cycle 5.

4.4. Behaviour of Cracks, Failure Mode, and Crack Pattern. The crack behaviour of all the beams under static and cyclic load is given in Table 7.

From Table 7, it is observed that the ultimate load-carrying capacity of BRGC beams under static and cyclic load is almost equal. But for GRGC and SRCC beams, the load-carrying capacity is lesser in cyclic load than the static load. The total number of cracks and crack spacing in all the beams under cyclic load is higher than those under static load at the ultimate load level. But at first crack load, the total number of cracks and spacing of cracks in BRGC and GRGC beams under cyclic load is less than those under static load compared with SRCC beams.

Compared to steel-reinforced control concrete beams, the crack propagation of FRP rods in geopolymer concrete beams are high due to the higher ductility of FRP bars for both static and cyclic loads. The observed crack spacing for BRGC-C, GRGC-C, and SRCC-C beams at ultimate load levels are 95 mm, 120 mm, and 85 mm, respectively, under cyclic load and for static load are 89 mm, 73 mm, and 71 mm, respectively. The average crack width at the ultimate load level decreases to 64%, 51%, and 73% BRGC-C, GRGC-C, and SRCC-C, respectively, compared with static load conditions.

The average crack width and propagation of all the beams under cyclic load is decreased compared with static load at the ultimate load level. But at first crack load, average crack width and the crack propagation for FRP beams are decreased compared with steel bars. The average crack width of FRP bars in geopolymer concrete is higher than the steel bars in control concrete under static and cyclic loading conditions.

The crack pattern and failure mode of BRGC-C, GRGC-C, and SRCC-C under cyclic load and BRGC-S, GRGC-S, and SRCC-S under static load are shown in Figure 8(a) and 8(b). Initially, the cracks are developed in the tension zone of the constant bending moment (CBZ) place, and then

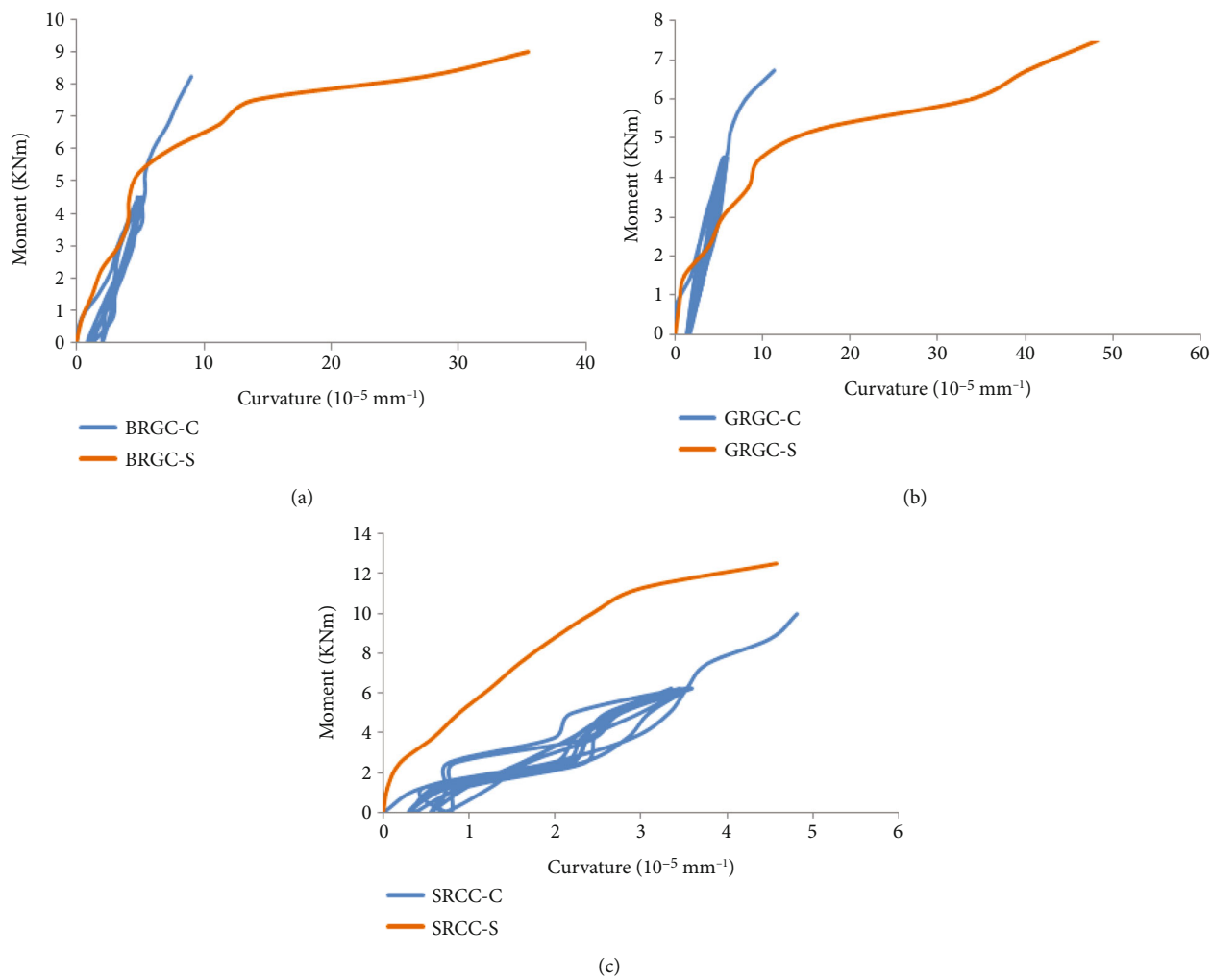

Figure 6: (a) Moment–curvature of BRGC beams. (b) Moment–curvature of GRGC beams. (c) Moment–curvature of SRCC beams.

new cracks are urbanised in other beams as load increases. The crack pattern for the beams of BRGC and GRGC bars under cyclic and static load is similar, i.e., pure shear failures have occurred. The sudden failure occurred after 95% of the ultimate load level reached cyclic and static loads. In SRGC beams, flexure and compression failure occurred.

4.5. Moment Capacity. During the experiment, the first crack appeared and the corresponding load were recorded for BRGC, GRGC, and SRCC beams under cyclic and static load. And also the ultimate moment attained for all the six beams was recorded. Bending moment at cracking state, ultimate state, and moment at serviceability state are given in Table 8.

4.5.1. Cracking Moment. The cracking moments were predicted using equation (2). A summary of the predicted cracking moments compared with the experimental results is shown in Table 9.

$$M_{cr} = \left(\frac{f_r}{y_t}\right) I_g, \tag{2}$$

$$f_r = 0.62\sqrt{f'_c} \text{ ACI (ACI committee, 2015)}, \tag{3a}$$

$$f_r = 0.6\sqrt{f'_c} \text{ ISIS (ISIS Manual, 2007)}, \tag{3b}$$

$$f_r = 0.4\sqrt{f'_c} \text{ CSA (CSA, 2014)}. \tag{3c}$$

When the applied moment reached the cracking moment capacity, a crack formed on the tension side of the beams and promulgated towards the top surface, the cracked concrete cannot carry tensile stress; this mainly causes a reduction in flexural rigidity.

4.5.2. Service State. The flexural strength at the service stage (Ms) indicates the performance of any Fibre-reinforced geopolymer concrete/steel-reinforced control concrete beam. Two criteria have been used to establish the service bending moment. The first criterion is from ISIS-07 [26], which defines the service moment as the applied moment corresponding to a tensile strain of 2000 $\mu\varepsilon$. Steel-reinforced concrete control beams have 1.33 and 2.22 times higher Ms capacity than Basalt and Glass reinforced geopolymer

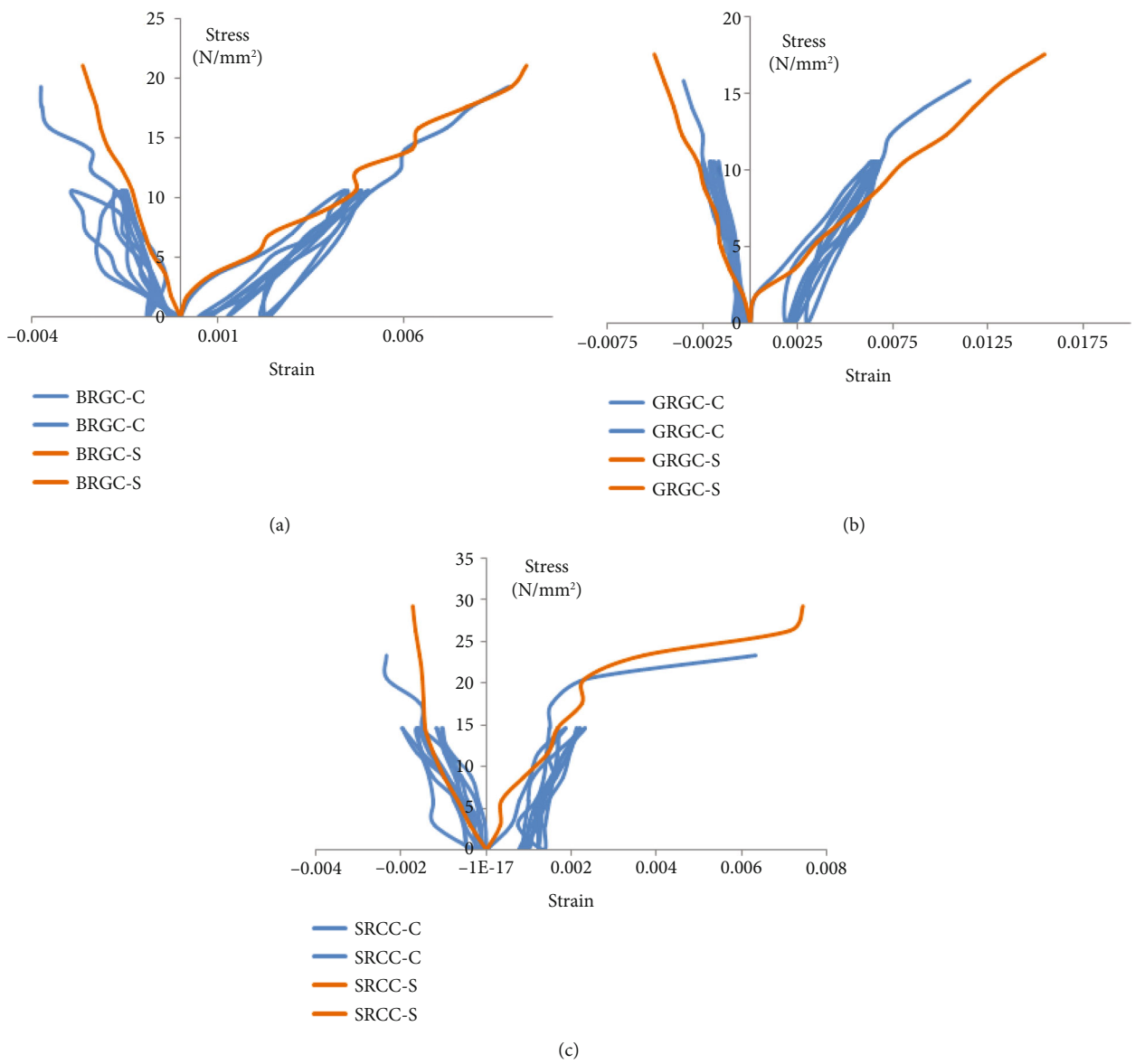

Figure 7: (a) Stress–strain behaviour of BRGC beams. (b) Stress–strain behaviour of GRGC beams. (c) Stress–strain behaviour of SRCC beams.

Table 6: Residual compressive and tensile strain for BRGC-C, GRGC-C, and SRCC-C beams under cyclic loads.

Cycles	BRGC-C		GRGC-C		SRCC-C	
	Residual strain (compression)	Residual strain (tension)	Residual strain (compression)	Residual strain (tension)	Residual strain (compression)	Residual strain (tension)
Cycle 1	0.00015	0.00049	0.00014	0.00193	0.00013	0.00078
Cycle 2	0.00022	0.00075	0.00035	0.00202	0.00014	0.00087
Cycle 3	0.00033	0.00124	0.00046	0.00217	0.00019	0.00100
Cycle 4	0.00086	0.00216	0.00066	0.00231	0.00026	0.00123
Cycle 5	0.00091	0.00231	0.00091	0.00298	0.00049	0.00136

concrete beams due to the larger modulus of steel bars' elasticity. Since the higher modulus of elasticity of BRGC beam, Ms capacity has 1.66 times higher than GRGC beams. The second criterion is Bischoff's [27] study, where the service moment is anticipated to be 30% of the ultimate moment (Mu). These estimations are comparable with each other.

Table 7: Behaviour of cracks under cyclic and static load.

Specimen ID	First crack load (KN)	Ultimate load (KN)	Total no of cracks-first (Nos)	Total no of cracks-ultimate (Nos)	Crack propagation-first (mm)	Crack propagation-ultimate (mm)	Spacing of cracks-first (mm)	Spacing of cracks-ultimate (mm)	Avg. crack width-first (mm)	Avg. crack width-ultimate (mm)
BRGC-C	6	34.80	7	18	70	127	110	95	0.02	0.2
GRGC-C	6	27.30	6	17	95	137	120	120	0.08	0.38
SRCC-C	15	44.55	6	15	72	106	153	85	0.03	0.08
BRGC-S	9	33.45	9	16	105	130	128	89	0.2	0.56
GRGC-S	6	32.4	6	13	135	153	197	73	0.24	0.78
SRCC-S	15	49.80	5	15	48	116	115	71	0.09	0.30

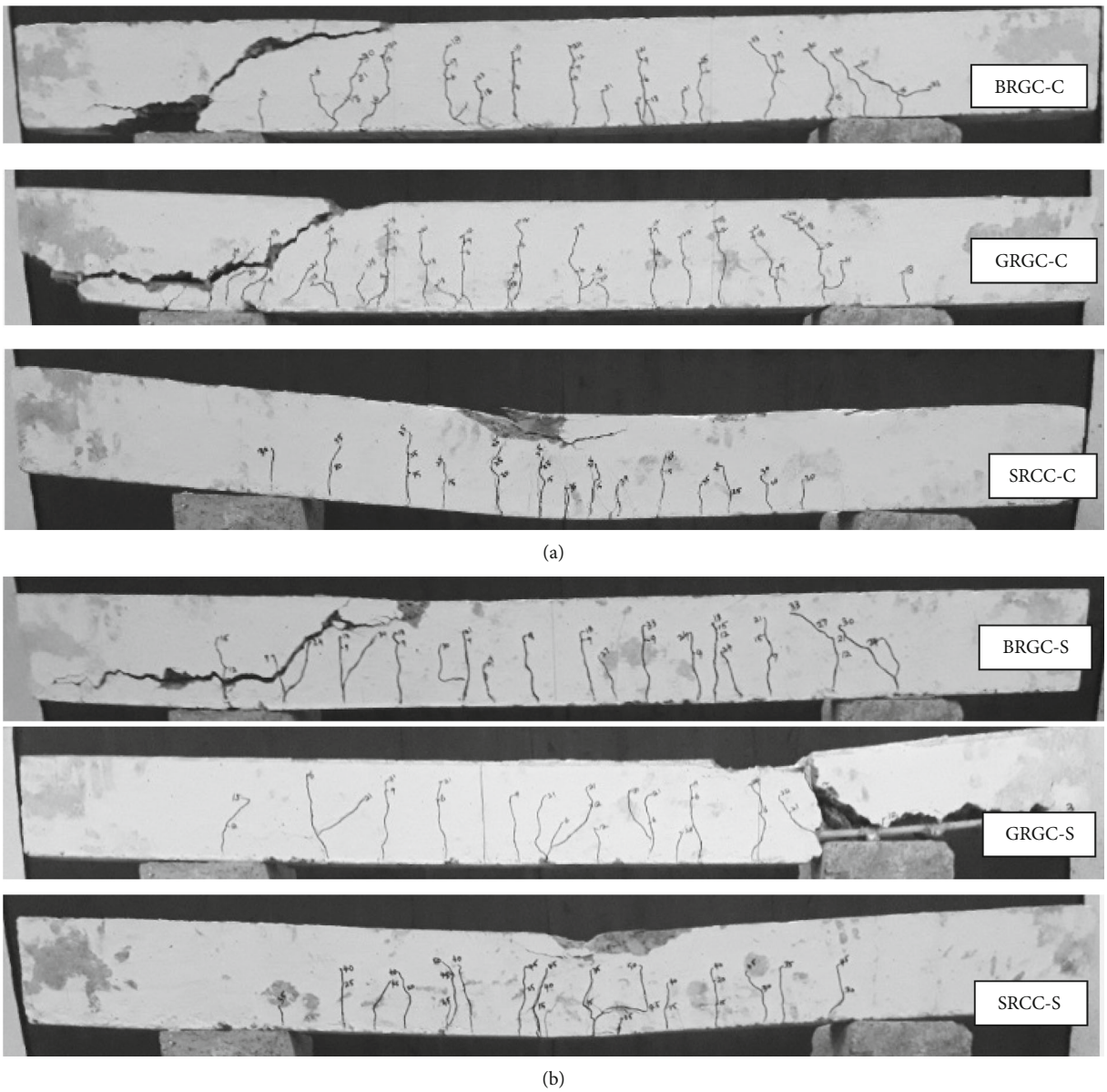

Figure 8: (a) Crack pattern and failure mode of BRGC-C, GRGC-C, and SRCC-C under cyclic load. (b) Crack pattern and failure mode of BRGC-S, GRGC-S, and SRCC-S under static load.

Table 8: Bending moment at cracking, ultimate and service state.

Specimen ID	Experimental moments (kNm)			
	Cracking moment (Mcr)	Ultimate moment (Mu)	Service moment 2000 $\mu\varepsilon$	(0.3 Mu)
BRGC-C	1.50	8.70	2.25	2.61
GRGC-C	1.50	6.83	1.5	2.05
SRCC-C	3.75	11.14	3.75	3.34
BRGC-S	2.25	8.36	3.75	2.51
GRGC-S	1.50	8.10	2.25	2.43
SRCC-S	3.75	12.45	5.00	3.74

Table 9: Experimental and predicted cracking moments.

Specimen ID	Experimental cracking moments (kNm)	Predicted cracking moments (kNm)		
		ACI	ISIS	CSA
BRGC-C	1.50	5.12	4.96	3.30
GRGC-C	1.50	5.12	4.96	3.30
SRCC-C	3.75	8.10	7.84	5.23
BRGC-S	2.25	6.27	6.07	4.05
GRGC-S	1.50	5.12	4.96	3.30
SRCC-S	3.75	8.10	7.84	5.23

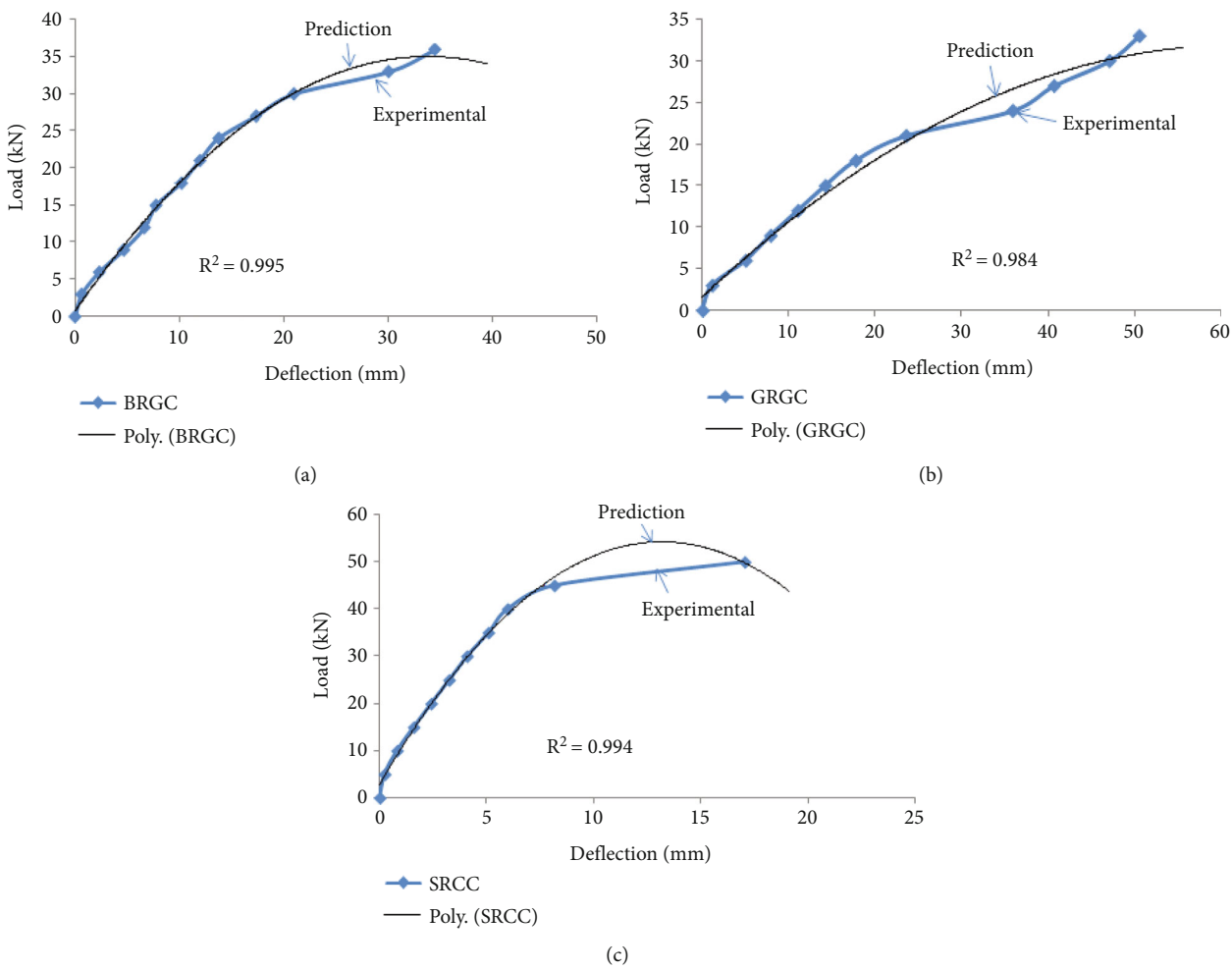

Figure 9: Correlation analysis between static load and deflection using multi variables regression (a) BRGC-S, (b) GRGC-S, (c) SRCC-S.

4.5.3. Ultimate Moment. The ultimate moment capacity of SRCC-C beams is only 1.28 and 1.63 times higher than BRGC-C and GRGC-C beams. Similarly, the ultimate moment capacity of SRCC-S beams is only 1.48 and 1.53 times higher than BRGC-S and GRGC-S beams.

5. Statistical Analysis for Static Load

Figure 9 represents the correlation analysis of static load and deflection of geopolymer concrete with FRP bars and control concrete with steel bars. Equations ((4a)–(4c)) are constructed to calculate

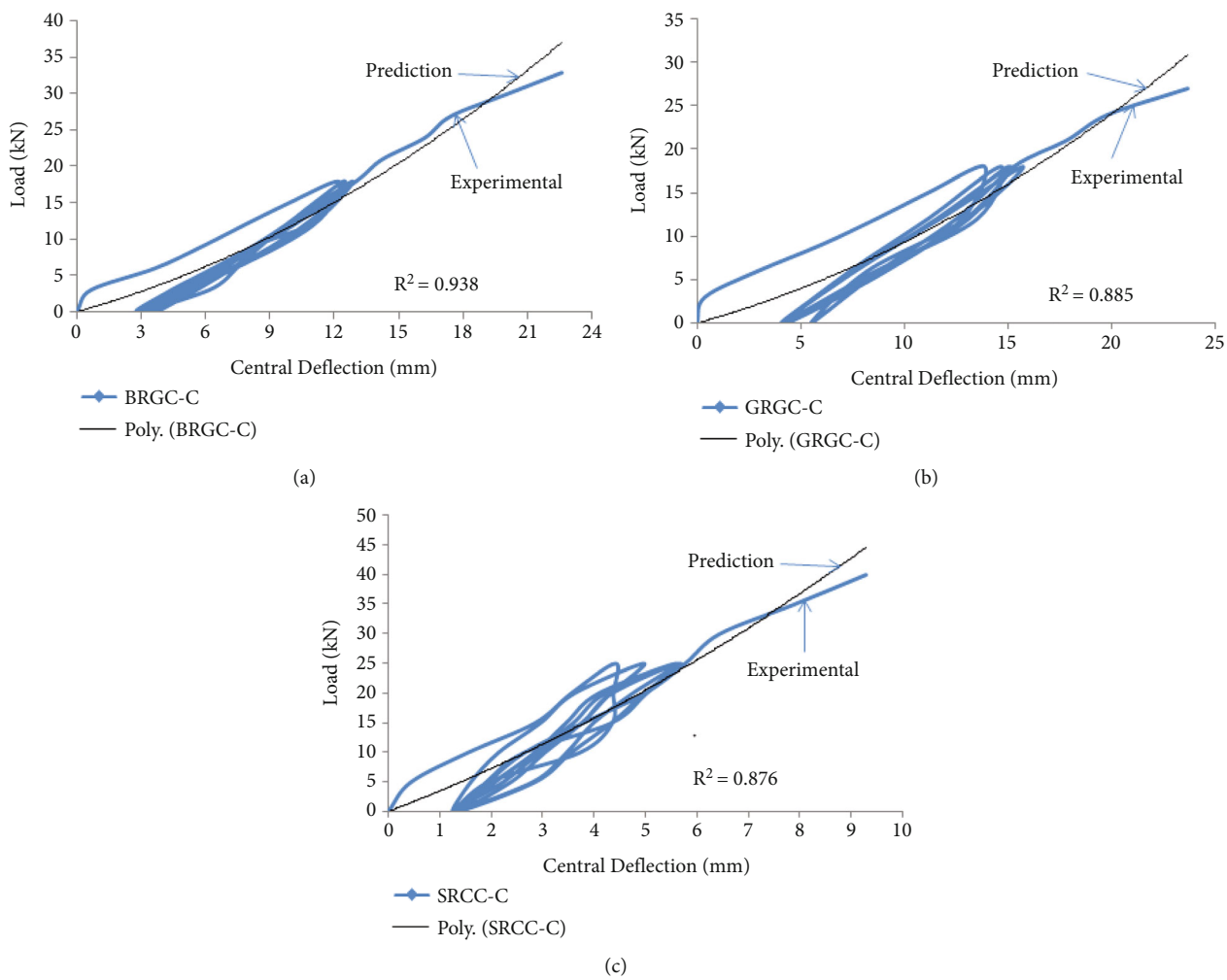

Figure 10: Correlation analysis between cyclic load and deflection using multi variables regression (a) BRGC-C, (b) GRGC-C, and (c) SRCC-C.

the load properties of geopolymer concrete and deflection using regression analysis (Nagajothi and Elavenil 2018).[32] The multi-viable regression statistical analysis results are specified in equations ((4a)–(4c)) for BRGC-S, GRGC-S, and SRCC-S, respectively.

$$P = 0.84 + 2.019\delta - 0.029\delta^2, \tag{4a}$$

$$P = 1.567 + 0.986\delta - 0.008\delta^2, \tag{4b}$$

$$P = 2.6 + 7.851\delta - 0.298\delta^2. \tag{4c}$$

Where P is the static load of the geopolymer and control concrete beam, δ is the deflection of geopolymer and control concrete for the applied load.

Considering equation (4a), Multiple factors 2.019 and −0.029 are observed along with different δ^2 values using multi-viable regression, and 0.84 is the constant value based on BRGC-S experimental results.

For GRGC-S and SRCC-S, a similar method was utilized to find forecast equations (4b) and (4c). The R^2 (correlation coefficient) values for equations (4a), (4b), and (4c) are 0.995, 0.984, and 0.994, respectively. A 100% accuracy was found between static load and deflection for BRGC-S, GRGC-S, and SRCC-S in correlation quality.

6. Statistical Analysis for Cyclic Load

Figure 10 represents the correlation analysis of cyclic load and deflection of geopolymer concrete with FRP bars and control concrete with steel bars. Equations ((5a)–(5c)) are constructed to calculate the load properties of geopolymer concrete and deflection using regression analysis. The statistical analysis results of multi-viable regression are specified in equations ((5a)–(5c)) for BRGC-C, GRGC-C, and SRCC-C, respectively.

$$P = 0.817\delta - 0.019\delta^2, \tag{5a}$$

$$P = 0.657\delta - 0.019\delta^2, \tag{5b}$$

$$P = 3.333\delta - 0.015\delta^2. \tag{5c}$$

Where P is the cyclic load of the geopolymer and control concrete beam and δ is the deflection of geopolymer and control concrete for the applied load.

Considering equation (5a), Multiple factors of 0.817 and –0.019 are observed along with different δ^2 values using multi-viable regression based on BRGC-C experimental results.

For GRGC-C and SRCC-C, a similar method was utilized to find forecast equations (5b) and (5c). The R^2 (correlation coefficient) values for equations (5a), (5b), and (5c) are 0.938, 0.885, and 0.876, respectively. The accuracy of correlation quality between cyclic load and deflection for BRGC-C, GRGC-C, and SRCC-C was found to be less compared with static load and deflection for BRGC-S, GRGC-S, and SRCC-S.

7. Conclusions

Six geopolymer and control concrete beams were tested under cyclic load compared with the static load. The following observations are derived from the experimental results for FRP bars in geopolymer concrete and steel bars in control concrete.

(i) The ultimate load-carrying capacity of GRGC-C and SRCC-C beam under cyclic load is decreased by 15.7% and 10.5%, respectively, compared with GRGC-S and SRCC-S beams under static load. But for the BRGC-C beam, cyclic load showed a trivial increase in the load-carrying capacity of the BRGC-S beam under static load.

(ii) The percentage reduction of deflection in BRGC-C, GRGC-C, and SRCC-C beams is 34.5%, 53.2%, and 45.8%, respectively, at the ultimate load level under cyclic load compared with the static load.

(iii) The BRGC and GRGC rods in geopolymer concrete would take more load than steel in cyclic and static loading conditions as a premature failure has occurred in FRP bars. It will be avoided by the closer spacing of shear reinforcement and increase in bond strength.

(iv) Based on the experimental values, multi-viable regression using statistical analysis and formulas was urbanized to resolve the static load-deflection and cyclic load-deflection behaviour of BRGC and GRGC in geopolymer concrete and SRCC in control concrete.

(v) The prediction equations recommended by ACI, ISIS, and CSA overestimated the cracking moments of the beams (tested), signifying a new prediction equation must be developed for FRP bars in geopolymer concrete beams. Further studies must be carried out to increase the approval of the proposed technology in the construction industry.

Data Availability

The data used to support the findings of this study are included within the article. Should further data or information be required, these are available from the corresponding author upon request.

Disclosure

The study was performed as a part of the Employment of Mettu University, Ethiopia.

Conflicts of Interest

The authors declare that there are no conflicts of interest regarding the publication of this paper.

Acknowledgments

The authors like to thank Dr. M. Neelamegam, Former Scientist of SERC-CSIR, Chennai, for his valuable suggestions and would like to acknowledge VIT, Chennai, India, for its work to carry out my research work.

References

[1] J. S. J. Van Deventer, J. L. Provis, and P. Duxson, "Technical and commercial progress in the adoption of geopolymer cement," *Minerals Engineering*, vol. 29, pp. 89–104, 2012.

[2] J. Xing, Y. Zhao, J. Qiu, and X. Sun, "Microstructural and mechanical properties of alkali activated materials from two types of blast furnace slags," *Materials*, vol. 12, no. 13, p. 2089, 2019.

[3] H. Y. Zhang, V. Kodur, S. L. Qi, L. Cao, and B. Wu, "Development of metakaolin-fly ash based geopolymers for fire resistance applications," *Construction and Building Materials*, vol. 55, pp. 38–45, 2014.

[4] A. Cherki El Idrissi, E. Rozière, S. Darson-Balleur, and A. Loukili, "Resistance of alkali-activated grouts to acid leaching," *Construction and Building Materials*, vol. 228, p. 116681, 2019.

[5] A. Gruskovnjak, B. Lothenbach, L. Holzer, R. Figi, and F. Winnefeld, "Hydration of alkali-activated slag: comparison with ordinary portland cement," *EMPA Activities*, vol. 18, no. 3, pp. 119–128, 2006.

[6] G. M. Zannerni, K. P. Fattah, and A. K. Al-Tamimi, "Ambient-cured geopolymer concrete with single alkali activator," *Sustainable Materials and Technologies*, vol. 23, article e00131, 2020.

[7] S. M. Hama and N. N. Hilal, "Fresh properties of self-compacting concrete with plastic waste as partial replacement of sand," *International Journal of Sustainable Built Environment*, vol. 6, no. 2, pp. 299–308, 2017.

[8] PCA, *Types and Causes of Concrete Deterioration*, Portland Cement Association, PCA R&D Se, 2002.

[9] B. Saikia, P. Kumar, J. Thomas, K. S. N. Rao, and A. RamaswamyStrength and serviceability performance of beams reinforced with GFRP bars in flexure," *Construction and Building Materials*, vol. 21, no. 8, pp. 1709–1719, 2007.

[10] M. M. Rafi, A. Nadjai, and F. Ali, "Experimental testing of concrete beams reinforced with carbon FRP bars," *Journal of Composite Materials*, vol. 41, no. 22, pp. 2657–2673, 2007.

[11] V. G. Kalpana and K. Subramanian, "Behavior of concrete beams reinforced with GFRP BARS," *Journal of Reinforced Plastics and Composites*, vol. 30, no. 23, pp. 1915–1922, 2011.

[12] M. Osama Ahmed, A. H. Waddah, and K. Mohammad, "Durability and mechanical properties of concrete reinforced sustainable infrastructure," *Polymers*, vol. 13, p. 1402, 2021.

[13] S. Nagajothi and S. Elavenil, "Strength assessment of geopolymer concrete using M-sand," *International Journal of Chemical Sciences*, vol. 14, pp. 115–126, 2016.

[14] Z. Wang, X. L. Zhao, G. Xian, G. Wu, R. K. S. Raman, and S. Al-Saadi, "Effect of sustained load and seawater and sea sand concrete environment on durability of basalt- and glass-fibre reinforced polymer (B/GFRP) bars," *Corrosion Science*, vol. 138, pp. 200–218, 2018.

[15] S. Karthiyaini and S. Nagan, "Behaviour of geopolymer concrete circular column using glass fiber reinforced polymer," *Indian Journal of Engineering and Materials Sciences*, vol. 21, no. 4, pp. 458–464, 2014.

[16] P. Sarker, "Bond strengths of geopolymer and cement concretes," *Advances in Science and Technology*, vol. 69, pp. 143–151, 2010.

[17] S. Nagajothi and S. Elavenil, "Influence of aluminosilicate for the prediction of mechanical properties of geopolymer concrete—artificial neural network," *Silicon*, vol. 12, no. 5, pp. 1011–1021, 2020.

[18] J. Sabzi, M. R. Esfahani, T. Ozbakkaloglu, and B. Farahi, "Effect of concrete strength and longitudinal reinforcement arrangement on the performance of reinforced concrete beams strengthened using EBR and EBROG methods," *Engineering Structures*, vol. 205, no. December 2019, p. 110072, 2020.

[19] G. M. Raftery and C. Whelan, "Low-grade glued laminated timber beams reinforced using improved arrangements of bonded-in GFRP rods," *Construction and Building Materials*, vol. 52, pp. 209–220, 2014.

[20] W. M. Shaban, J. Yang, H. Su, K. H. Mo, L. Li, and J. Xie, "Quality improvement techniques for recycled concrete aggregate: a review," *Journal of Advanced Concrete Technology*, vol. 17, no. 4, pp. 151–167, 2019.

[21] M. S. H. Khan, A. Castel, A. Akbarnezhad, S. J. Foster, and M. Smith, "Utilisation of steel furnace slag coarse aggregate in a low calcium fly ash geopolymer concrete," *Cement and Concrete Research*, vol. 89, pp. 220–229, 2016.

[22] M. M. Islam, M. A. Chowdhury, M. A. Sayeed, E. HossainAl, S. S. Ahmed, and A. Siddique, "Finite element analysis of steel fiber-reinforced concrete (SFRC): validation of experimental tensile capacity of dog-bone specimens," *International Journal of Advanced Structural Engineering*, vol. 6, no. 3, pp. 1–8, 2014.

[23] Y. Lu, T. Zhu, S. Li, and Z. Liu, "Bond behavior of wet-bonded carbon fiber-reinforced polymer–concrete interface subjected to moisture," *International Journal of Polymer Science*, vol. 2018, p. 11, 2018.

[24] N. Baša, M. Ulićević, and R. Zejak, "Experimental research of continuous concrete beams with GFRP reinforcement," *Advances in Civil Engineering*, vol. 2018, p. 16, 2018.

[25] N. K. Banjara and K. Ramanjaneyulu, "Investigations on behaviour of flexural deficient and CFRP strengthened reinforced concrete beams under static and fatigue loading," *Construction and Building Materials*, vol. 201, pp. 746–762, 2019.

[26] J. Newhook and D. Svecova, *Reinforcing Concrete Structures with Fibre Reinforced Polymers*, vol. 151, Can. ISIS Can. Corp, 2007, Design Manual No. 3.

[27] P. Bischoff, S. Gross, and C. Ospina, *The Story Behind Proposed Changes to ACI 440 Deflection Requirements for FRP-Reinforced Concrete*, vol. 264, pp. 53–76, 2009, Spec. Publ.

[28] ACI Committee 440, *Guide for the Design and Construction of Concrete Reinforced with FRP Bars (ACI 440.1R-15)*, American Concrete Institute, Farmington Hills, MI, 2015.

[29] Canadian Standard Assiociation (CSA), *Canadian Highway Bridge Design Code*, CAN/CSA S807-10, Rexdale, ON, Canada, 2010.

[30] ISIS Manual No.3, *Reinforced Concrete Structures with Fibre -Reinforced Polymers*, University of Manitoba, ISIS Canada Research Network, Winnipeg, MB, 2007.

[31] S. Nagajothi and S. Elavenil, "Flexural behaviour of geopolymer concrete beams reinforced with BFRP and GFRP polymer composites," *Advances in Structural Engineering*, pp. 1–12, 2022.

[32] S. Nagajothi and S. Elavenil, "Compressive Strength of Geopolymer Concrete using Taguchi Method," *International Journal of Pure and Applied Mathematics*, vol. 118, no. 24, pp. 1–10, 2018.

Hindawi
International Journal of Polymer Science
Volume 2021, Article ID 4935642, 7 pages
https://doi.org/10.1155/2021/4935642

Research Article

Cefuroxime-Loaded Hydrogels for Prevention and Treatment of Bacterial Contamination of Open Wounds

Pavlo Virych, Oksana Nadtoka, Volodymyr Doroschuk, Sergey Lelyushok, Vasyl Chumachenko, Tetiana Bezugla, and Nataliya Kutsevol

Taras Shevchenko National University of Kyiv, 64/13, Volodymyrska St, Kyiv 01601, Ukraine

Correspondence should be addressed to Pavlo Virych; sphaenodon@ukr.net

Received 12 July 2021; Revised 9 September 2021; Accepted 16 October 2021; Published 8 November 2021

Academic Editor: Deepa Kodali

Dextran/Sulfodextran-graft-polyacrylamide- and polyacrylamide-based hydrogels were synthesized by radical polymerization and loaded with cefuroxime to obtain antimicrobial wound dressings. Antibiotic release from the antibiotic-loaded hydrogels into an aqueous solution was studied by the HPLC-UV method. It is shown that cefuroxime-loaded Dextran/Sulfodextran-graft-polyacrylamide hydrogels release the antibiotic more slowly compared to polyacrylamide hydrogel with the same density of cross-links. Antibacterial activity of the synthesized materials was tested *in vitro* against wild strains of *S. aureus*, *E. coli*, and *Klebsiella* spp. The possibility of using the obtained antimicrobial hydrogels for the treatment of infected wounds was confirmed *in vivo* in a rat model.

1. Introduction

Among the many antibacterial agents, antibiotics are the most effective and widely used drugs. However, their widespread and often thoughtless use has provoked the emergence and expansion of resistant strains of bacteria. There are two main ways to overcome antibiotic resistance: the synthesis of novel antibiotics and the development of new methods of antibiotic applications. Hydrogels of different chemical nature appear to be promising carriers of antibiotics in biotechnology and medicine. Over the last few decades, various antibiotic-loaded hydrogels have been developed as antibacterial coatings and dressings for the treatment of superficial trauma, burn, or diabetic wounds [1–5]. These materials release antibiotics at the wound site, thus preventing infection and promoting the healing process [6]. Local administration of antibiotics significantly reduces the unwanted side effects that are often observed with systemic use.

Hydrogels are three-dimensional cross-linked polymer systems possessing high water swellability. The use of hydrogels as wound dressings or coverings requires some special properties such as biocompatibility, oxygen permeability, sufficient mechanical strength and flexibility, and the ability to be easily applied and removed from wounds [7, 8]. Multiple hydrophilic groups of hydrogels ensure nonadhesion to the wound, which means painless removal of the coating. They also create a moist wound environment that is beneficial for healing [9]. Currently, various hydrogels are extensively studied as drug delivery systems, and some of them have already been used as wound dressings. The researchers highlight the advantages of hydrogels over traditional pharmaceuticals [2, 10].

Topical administration of antimicrobials allows formulating the hydrogels that contain high concentrations of antibiotics [9]. It is especially important for the care of infected wounds and burns. Sometimes, antibiotic-loaded hydrogels are tested against both antibiotic-susceptible and antibiotic-resistant bacteria [11, 12].

The hydrogels loaded with antibiotics must release the active substance in a sustained manner because successful anti-inflammatory wound treatment is directly dependent on the continuous action of antimicrobial agents. Controlled and prolonged release of the antibiotic in the affected area is the essential requirement for the prevention of biofilm formation [6, 13]. Moreover, sustained delivery of the drug to

the application site ensures a significant increase in time intervals needed to change the dressing on the wound. The nature of the polymer and the degree of cross-linking are believed to be the main factors that regulate the ability of hydrogels to deliver drug substances and release them at the target site. Some structure peculiarities of hydrogels can affect these processes too.

Our idea was to create polyacrylamide-based antimicrobial hydrogels for the treatment of infected wounds. These hydrogels can be loaded with the desired amount of antibiotics, and their local application for drug release provides overcoming the side effects of a systemic overdose. To vary the structure of the synthesized hydrogels, small amounts of polysaccharides were used in the syntheses as structure-affecting components. The antibiotic-loaded samples were tested *in vitro* against some painful bacteria and *in vivo* as antimicrobial dressings.

2. Materials and Methods

2.1. Reagents. Acrylamide (AA), three samples of Dextran with $M_w = 20\,000$ g/mol (D20), $M_w = 100\,000$ g/mol (D100), and $M_w = 500\,000$ g/mol (D500), Sulfodextran with $M_w = 500\,000$ g/mol (SD500), N,N′-methylene-bis-acrylamide (MBA), and cerium (IV) ammonium nitrate (CAN) were supplied by Sigma-Aldrich (USA). Antibiotic cefuroxime and antiseptic miramistin were purchased at a local pharmacy.

All reagents were used without further purification. Double-deionized water was used for all syntheses and procedures.

2.2. Syntheses of Hydrogels. Dextran/Sulfodextran-graft-polyacrylamide (D/SD-g-PAA) hydrogels were synthesized by free-radical polymerization in the presence of MBA as a cross-linker (Figure 1) [14, 15]. Being added into the synthesis mixture in very small amounts, Dextran/Sulfodextran affected the structure of the final product.

Dextran/Sulfodextran (5×10^{-4} mmol) was dissolved in 24 mL of distilled water at 25°C. The polysaccharide solution was stirred and bubbled with argon for 20 min to remove oxygen. Then, a CAN/HNO_3 initiator system (3×10^{-2} mmol CAN in 1 mL of 0.125 N HNO_3) was added, and the solution was stirred and bubbled with argon for another 2 min. A monomer AA (50 mmol) and a cross-linking agent MBA (0.4 g per 100 g of AA) were added to the solution. The reaction mixture was kept under argon for 24 h. To remove the unreacted monomer, the obtained hydrogels were thoroughly washed with distilled water. Then, all samples were dried and stored at ambient temperature.

Polyacrylamide (PAA) hydrogels were synthesized under the same conditions but without the Dextran/Sulfodextran in the reaction mixture. The samples of cross-linked PAA were dried and stored as the samples of cross-linked D/SD-g-PAA.

Further in the text, the synthesized hydrogels are designated as D20-g-PAA-0.4, D100-g-PAA-0.4, D500-g-PAA-0.4, and SD500-g-PAA-0.4 according to a polysaccharide component of the obtained samples and a ratio MBA to AA in the syntheses.

2.3. Preparation of Antibiotic-Loaded Hydrogels. The weighed samples of the dried hydrogels were placed in an aqueous solution of cefuroxime (166.6 mg/mL) and incubated at 25°C for 18 hours. The amount of loaded antibiotic in the hydrogel sample was estimated by subtracting the amount of cefuroxime remaining in the solution from the initial content. All concentrations were determined by high-performance liquid chromatography with ultraviolet detection (HPLC-UV). The hydrogels swollen in this solution were used for further studies of their ability to release the antibiotic. Such samples contain an indication of cefuroxime (-Cef) in their names.

2.4. Antibiotic Release Study. The swollen samples of the antibiotic-loaded hydrogels were removed from the solution of cefuroxime, wiped with a piece of filter paper, and then placed in 25.0 mL of distilled water. The experiment was performed with gentle stirring at 25°C. To determine the concentration of the antibiotic released into the solution, the aliquots of the solution were taken at regular intervals and analyzed by the HPLC-UV method. The antibiotic release experiment was performed with each antibiotic-loaded hydrogel at least three times.

2.5. Thermogravimetric Analysis (TGA). Thermogravimetric studies of the synthesized hydrogels were performed using a Netzsch TG 209 F1 Libra apparatus (Selb, Germany). The experiments were carried in a nonisothermal mode. Dry samples were heated with the heating rate of 10°C/min and monitored for weight change in the range of 30-900°C. The measurements were carried out under nitrogen protective flow. The weight of the samples under investigation was 10 mg. Al_2O_3 served as reference material.

2.6. In Vitro Tests for Antibacterial Activity. To test the antibacterial hydrogels for their ability to inhibit bacterial growth, wild-type strains of *Staphylococcus aureus*, *Escherichia coli*, and *Klebsiella* spp. selectively grown on Endo's or yolk-salt agar media were used. The sensitivity of the microorganisms was evaluated by the disc diffusion method on a Müller–Hinton agar of the following composition (g/L): agar—17, hydrolyzed casein—17.5, hydrolyzed bovine hart—2, and water-soluble starch—1.5; pH = 7.3. The dry hydrogels were swollen (24 h) in an aqueous solution of cefuroxime (0.1 and 1 mg/mL). A miramistin solution (0.1 mg/mL) was used for the control experiment. The tested samples were 5 mm in diameter, and their sizes were similar to those of standard disks with antibiotics. The measurement of the growth inhibition zone was carried out using a digital caliper Miol 15-240. The contact of the hydrogel samples with the microorganisms occurred within 24 h before recording the diameter of growth inhibition. Statistical data processing was performed using the Shapiro-Wilk test ($p > 0.05$) and the Scheffe ANOVA test ($p < 0.05$). Each *in vitro* experiment was repeated three times.

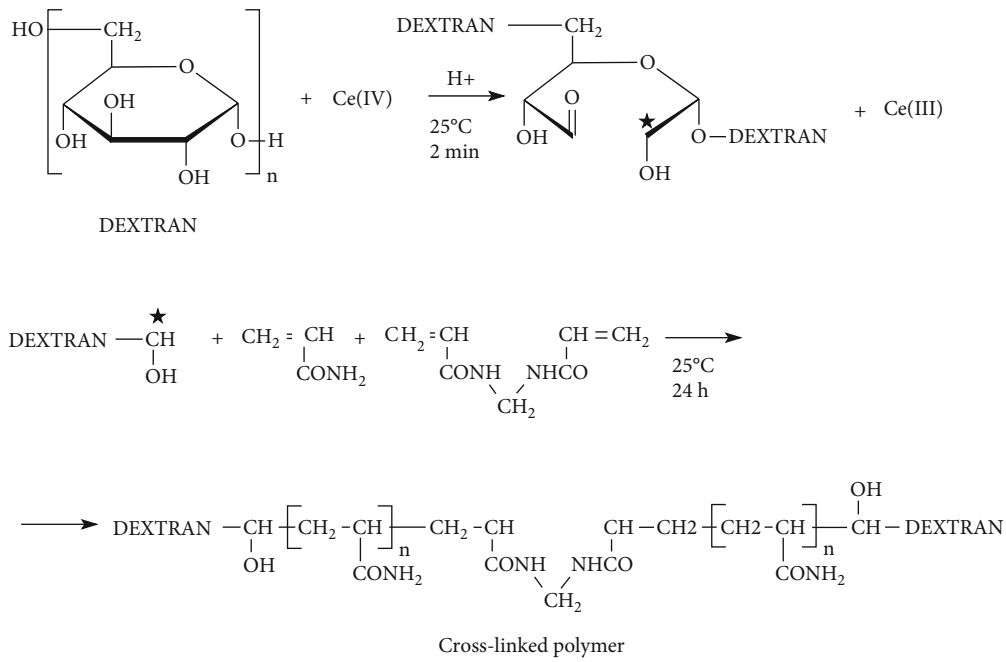

Figure 1: The proposed mechanism of the synthesis of cross-linked D-g-PAA hydrogels.

2.7. In Vivo Evaluation of Healing Properties. The effects of synthesized antibacterial hydrogels on infected wound healing were assessed by the rat wound model. The *in vivo* tests were performed using white outbred rats, which were kept in standard conditions of a vivarium. All manipulations with animals were carried out according to the Law of Ukraine "On the Protection of Animals from Cruelty" and the European Convention for the Protection of Vertebrate Animals Used for Research and Other Scientific Purposes.

Female rats weighing 230-260 g were selected, and general anesthesia was performed with sodium etaminal at the rate of 3.5 mg per 1 kg of live weight. The area of the back between the shoulder blades of the animal was cleared of hair. A section of skin 7-8 mm in diameter was removed with a sharp scalpel. The resulting wound was infected with the mixture of microorganisms *S. aureus*, *E. coli*, and *Klebsiella* spp., which were in physiological solution in the amount of $1{\cdot}10^8$ CFU/mL. The wound was covered with the synthesized hydrogels loaded with cefuroxime (1 mg/mL) or miramistin (0.1 mg/mL) and the standard fabric material (gauze dressing). The bandage was fixed with a wide Band-Aid. After 24 h, the wound was wiped with a sterile swab, and the wound bacteria were inoculated into the nutrient medium. Yolk-saline agar was used to cultivate gram-positive bacteria, and Endo's medium was used for gram-negative bacteria.

Wound healing of the rats was assessed visually.

Skin irritation tests revealed that D/SD-g-PAA hydrogels per se did not cause any irritation, indicating its safety for topical application.

3. Results and Discussion

The syntheses of the cross-linked Dextran (Sulfodextran)-graft-polyacrylamide hydrogels include two stages: (1) the preparation of polysaccharide macroradicals as a result of Dextran/Sulfodextran interaction with CAN/HNO_3 oxidative system [16, 17] and (2) the growth of PAA chains from active centers on the polysaccharide and their simultaneous cross-linking by the MBA cross-linking agent (Figure 1). Since the concentration of the cross-linking agent MBA is the same in all syntheses, it is assumed that the density of cross-links in all hydrogels is the same.

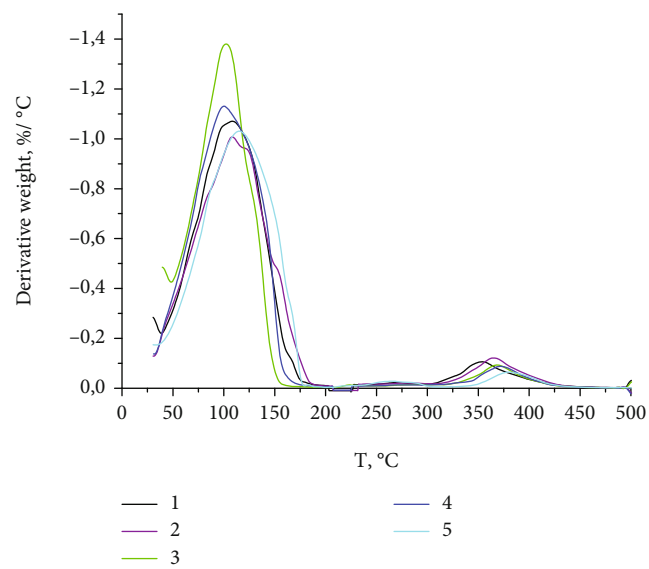

Figure 2: Derivative weight loss curve vs. temperature: (1) PAA-0.4, (2) D20-g-PAA-0.4, (3) D100-g-PAA-0.4, (4) D500-g-PAA-0.4, and (5) DS500-g-PAA-0.4 hydrogels.

As shown earlier [18], the number of grafted polyacrylamide chains in the synthesized D(SD)-g-PAA copolymers is determined by the molar ratio of the polysaccharide and

Table 1: Temperature intervals of weight loss on heating, obtained by the DTA method.

	Sample	Peak 1	Peak 2
1	D20-g-PAA-0.4	35-190	315-485
2	D100-g-PAA-0.4	45-160	320-450
3	D500-g-PAA-0.4	30-180	330-450
4	DS500-g-PAA-0.4	30-185	350-480
5	PAA-0.4	35-190	300-470

Table 2: Content of cefuroxime in the synthesized hydrogels (g of antibiotic per g of dried hydrogel).

	Sample	Content (g/g)
1	D20-g-PAA-0.4-Cef	3.52
2	D100-g-PAA-0.4-Cef	3.40
3	D500-g-PAA-0.4-Cef	3.34
4	DS500-g-PAA-0.4-Cef	3.31
5	PAA-0.4-Cef	1.64

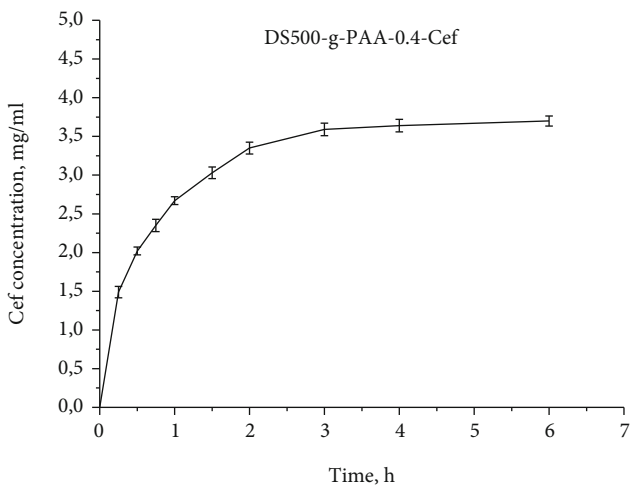

Figure 3: Cefuroxime concentration in water solution vs. time of contact with DS500-g-PAA-0.4-Cef hydrogel.

the CAN initiator. Formed under the action of the initiator, the active centers on the polysaccharide macromolecule trigger the growth of polyacrylamide chains. According to the molar ratio of Dextran (Sulfodextran) to CAN used in the syntheses of hydrogels described above, approximately 60 points of growth can appear on the polysaccharide macromolecule. Near the grafting point, the growing polyacrylamide chains have a conformation that essentially differs from those for PAA macromolecules in solution [16, 19]. An increase in the molecular weight of Dextran molecules, as well as the appearance of a charge on the polymer chain of Sulfodextran, has a significant effect on the conformation of the growing polyacrylamide chain in the nearest vicinity of the polysaccharide. Thus, the internal structure of the cross-linked D/SD-g-PAA hydrogels and their properties may differ from the structure and properties of cross-linked PAA with the same number of cross-links.

Table 3: Release of cefuroxime (in %) from the antibiotic-loaded hydrogels into water.

	Sample	Time of contact		
		0.5 h	1 h	6 h
1	PAA-0.4-Cef	28.2 ± 1.5	41.6 ± 3.1	55.1 ± 2.7
2	D20-g-PAA-0.4-Cef	24.4 ± 2.3	29.6 ± 2.1	41.9 ± 1.6
3	D100-g-PAA-0.4-Cef	22.1 ± 2.3	27.0 ± 2.2	38.1 ± 2.4
4	D500-g-PAA-0.4-Cef	18.6 ± 2.7	33.9 ± 2.1	39.5 ± 2.7
5	DS500-g-PAA-0.4-Cef	27.9 ± 2.5	37.2 ± 2.0	50.6 ± 2.7

Table 4: Antimicrobial activity of cefuroxime-loaded hydrogels swollen in 1 mg/mL antibiotic solution.

	Sample	Diameter of the growth inhibition zone (mm)		
		S. aureus	*E. coli*	*Klebsiella* sp.
1	PAA-0.4-Cef	27.1 ± 1.5	23.2 ± 2.8	20.1 ± 2.4
2	D20-g-PAA-0.4-Cef	26.0 ± 2.4	21.1 ± 3.0	20.3 ± 2.4
3	D100-g-PAA-0.4-Cef	29.8 ± 2.1	21.8 ± 2.7	20.2 ± 2.5
4	D500-g-PAA-0.4-Cef	25.2 ± 2.5	22.1 ± 2.8	22.7 ± 2.4
5	DS500-g-PAA-0.4-Cef	29.1 ± 2.5	21.3 ± 2.7	22.0 ± 2.8

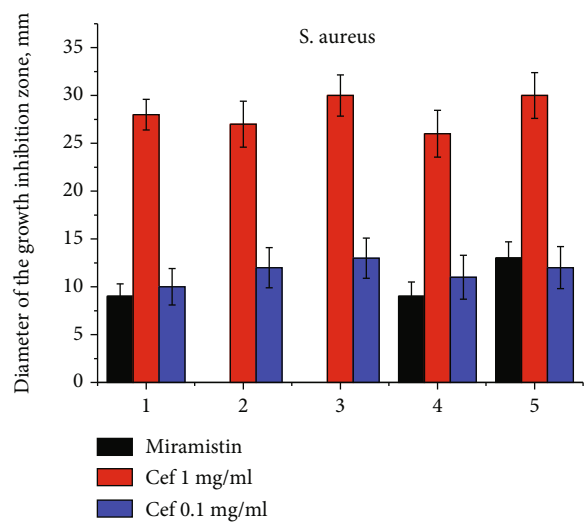

Figure 4: Activity of the antimicrobial hydrogels (1) PAA-0.4-Cef, (2) D20-g-PAA-0.4-Cef, (3) D100-g-PAA-0.4-Cef, (4) D500-g-PAA-0.4-Cef, and (5) DS500-g-PAA-0.4-Cef against *S. aureus* (black—miramistin 0.1 mg/mL; blue—cefuroxime 0.1 mg/mL; red—cefuroxime 1 mg/mL).

According to thermogravimetric data, all synthesized hydrogels are very hydrophilic and contain water even when dried. The first weight loss step is registered in the range of 40-190°C with a maximum of about 100°C indicating water desorption (Figure 2). In addition, in this interval at higher temperatures, the elimination of NH_3 and CO can occur as a result of chemical reactions between some neighboring functional groups of the polyacrylamide chains [20]. The second distinct weight loss step is observed at 300-485°C with a rather

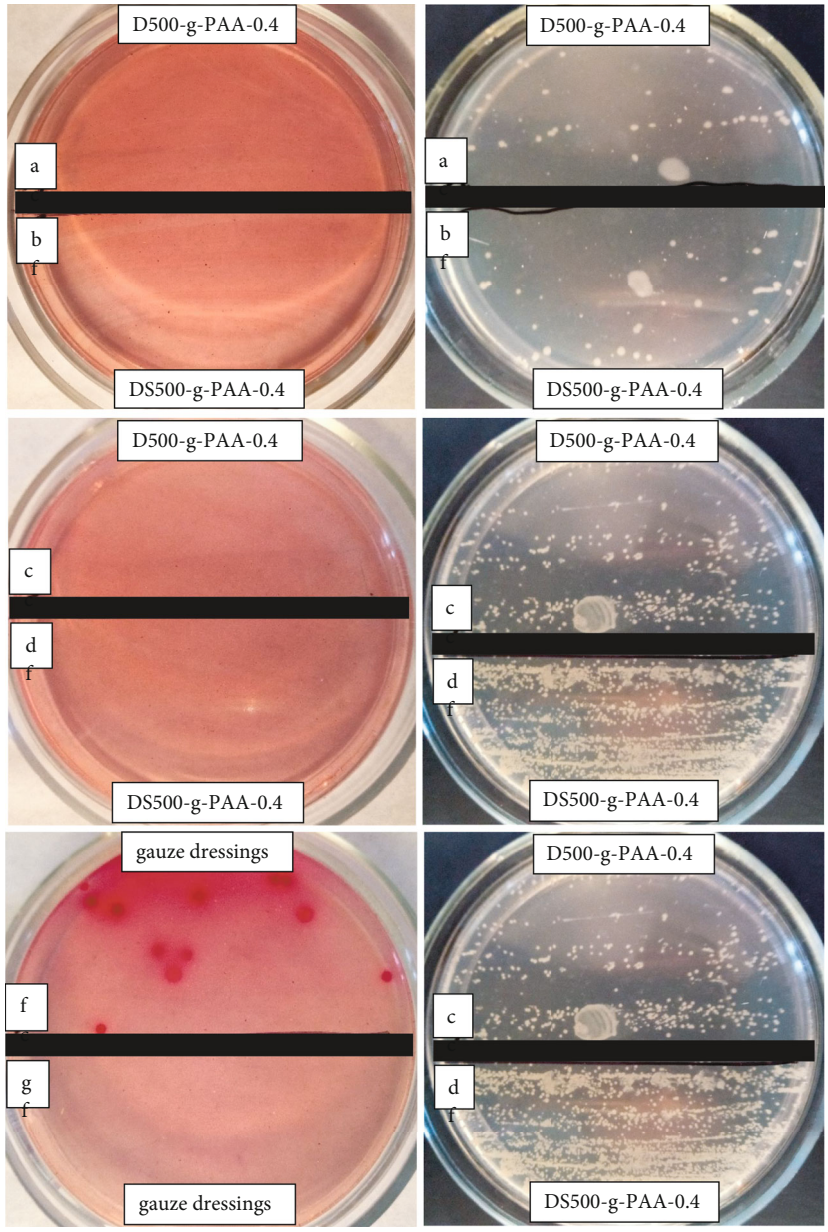

Figure 5: Cultivation of bacteria using Endo (left) and yolk-salt (right) agar media after removal of (a, b) cefuroxime-loaded hydrogels from infected wound; (c, d) miramistin-loaded hydrogels; (f, g) gauze dressings.

lower maximum on the derivative weight loss curve. It corresponds to the decomposition of the polymer matrix itself, which consists mainly of polyacrylamide fragments. The destruction of the polymer matrix of D/SD-g-PAA-0.4 samples begins at a higher temperature compared to PAA-0.4. The increase in this temperature is 15-50°C, depending on the internal structure of the hydrogels (Table 1).

To prepare the antibiotic-loaded hydrogels for drug release studies, the samples of the dry hydrogels were swollen in an aqueous solution of cefuroxime for 18 h. As shown in Table 2, the content of cefuroxime is the greatest for the hydrogels that were synthesized using Dextrans as a structure-affecting component.

The contact of the synthesized antibiotic-loaded hydrogels with water leads to the desorption of drug molecules into the solution. A typical antibiotic release profile is shown in Figure 3. For all samples, the initial burst of release is followed by desorption at a slower rate. After 3 hours, only a slight increase in the concentration of cefuroxime in the solution can be registered. The sample PAA-0.4-Cef was found to have the highest release rate; the content of cefuroxime in this hydrogel decreased by 55% after 6 h of contact with water (Table 3). The behavior of D-g-PAA-0.4-Cef hydrogels in this process is somewhat different. Being initially more loaded with cefuroxime, these samples release the drug into solution more slowly than PAA-0.4-Cef.

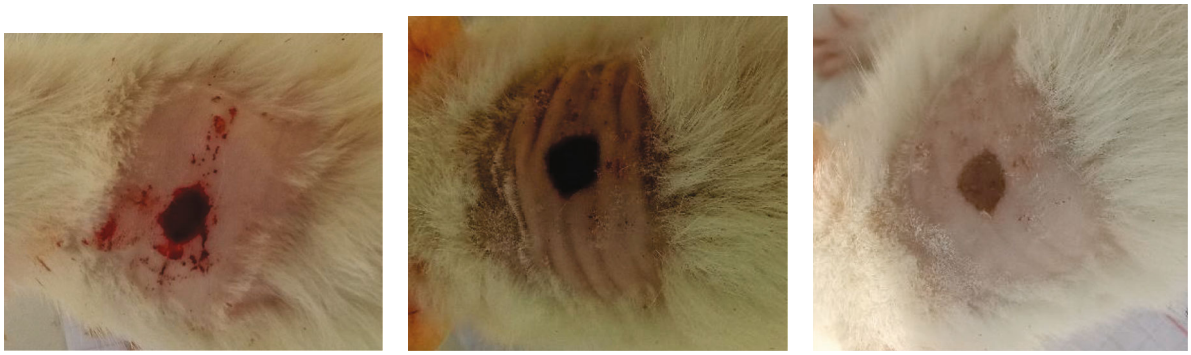

(a) (b) (c)

Figure 6: Rat wounds after removal of bandages (24 h): (a) classic gauze dressing (the wound was opened after the animal's motor activity); (b) miramistin-loaded D500-g-PAA-0.4 hydrogel; (c) cefuroxime-loaded D500-g-PAA-0.4 hydrogel.

Thus, D/DS-g-PAA-0.4-Cef hydrogels have some advantages over other hydrogels under investigation. They are assumed to be promising biomaterials for topical application as antimicrobial dressings with prolonged action.

To compare the antimicrobial activity of the antibiotic-loaded hydrogels with different internal structures, the dry samples were swollen in an aqueous solution of cefuroxime (0.1 or 1 mg/mL) for 24 h. Miramistin was used as cargo for control experiments. All synthesized cefuroxime-loaded hydrogels demonstrate high activity against test bacterial strains of *S. aureus*, *E. coli*, and *Klebsiella* spp. The diameter of the growth inhibition zone is 25-30 mm for *S. aureus* and 20-23 mm for *E. coli* and *Klebsiella spp*. when using the hydrogel samples prepared by swelling in a solution of cefuroxime with a concentration of 1 mg/mL (Table 4).

The antimicrobial activity is dose-dependent, but even at a low dose, antibiotic-loaded hydrogels demonstrate high efficacy against harmful microorganisms (Figure 4).

The *in vivo* study of the activity of the synthesized antibiotic-loaded hydrogels against infections was carried out on a rat wound model. Rat models are widely used to investigate various treatments for living organisms [21, 22]. To evaluate the possibility of using antibiotic-loaded D/SD-g-PAA hydrogels in wound protecting and healing, two hydrogels D500-g-PAA-0.4 and SD500-g-PAA-0.4 were swollen in cefuroxime solution (1 mg/mL), and then, they were used to cover the infected wounds of rats. After 24 hours, the bandage was removed from the infected wound, and the surface material of the wound was scraped off. Inoculation of scraping microorganisms on a nutrient medium shows the complete absence of gram-negative bacteria (Figures 5(a) and 5(b), left) and very few colonies of gram-positive colonies (Figures 5(a) and 5(b), right) after 24 h of their growth. According to obtained data, the studied cefuroxime-loaded hydrogel samples demonstrate a higher effectiveness against bacteria compared to the miramistin-loaded hydrogels (Figures 5(c) and 5(d)) and especially to classic gauze dressings (Figures 5(f) and 5(g)).

The cefuroxime-loaded D/SD-g-PAA hydrogels demonstrated their efficacy against a mixture of pathogenic bacteria, so they can be used topically as antimicrobial dressings. The *in vivo* experiments show that these antimicrobial hydrogels substantially inhibit the growth of microorganisms on an infected wound surface. The appearance of the rat wounds after removing the bandage confirms the promising use of antibiotic-loaded hydrogels as biomaterials that provide good healing of superficial wounds (Figure 6).

4. Conclusions

D/SD-g-PAA-based hydrogels are promising materials for the development of antimicrobial dressings for the protection and treatment of superficial wounds. As shown, the structure of hydrogels can be controlled at the stage of synthesis. These hydrogels can be loaded with the desired amount of antibiotics, ensuring that the drug is delivered to the desired site without systemic overdose. The synthesized antimicrobial hydrogels can be prepared in the shape and size required for the wound. It has been shown that the release of the antibiotic is slower for antibiotic-loaded D/SD-g-PAA hydrogels compared to PAA-based hydrogel with the same number of cross-links, which is beneficial for wound healing. Testing of cefuroxime-loaded hydrogels on infected rat wounds has shown rapid clearance and healing of the infected wounds.

Data Availability

Data are available on request. To take data, please write to the corresponding author.

Conflicts of Interest

The authors declare that they have no conflicts of interest.

Acknowledgments

This publication is supported in part by the Ministry of Education and Science of Ukraine, Project (2019-2021), "Fundamental principles of creating nanohybrid functional composites synthesized in polymer matrices capable to response to external stimuli" and by the National Research Foundation of Ukraine, Project 2020.02/0022, "Plasmon hybrid nanosystems "metal-polymer-fluorophore" with enhanced optical response for

photonics and biomedical applications" and Grant of the Ministry of Education and Science of Ukraine for perspective development of a scientific direction "Mathematical sciences and natural sciences" at Taras Shevchenko National University of Kyiv.

References

[1] S. Veiga and J. P. Schneider, "Antimicrobial hydrogels for the treatment of infection," *Biopolymers*, vol. 100, no. 6, pp. 637–644, 2013.

[2] S. Li, S. Dong, W. Xu et al., "Antibacterial hydrogels," *Advanced science (Weinheim, Baden-Wurttemberg, Germany)*, vol. 5, no. 5, p. 1700527, 2018.

[3] A. S. Zakaria, S. A. Afifi, and K. A. Elkhodairy, "Newly developed topical cefotaxime sodium hydrogels: antibacterial activity and in vivo evaluation," *BioMed Research International*, vol. 2016, 2016.

[4] H. Namazi, R. Rakhshaei, H. Hamishehkar, and H. S. Kafil, "Antibiotic loaded carboxymethylcellulose/MCM-41 nanocomposite hydrogel films as potential wound dressing," *International Journal of Biological Macromolecules*, vol. 85, pp. 327–334.

[5] V. Pawar, M. Dhanka, and R. Srivastava, "Cefuroxime conjugated chitosan hydrogel for treatment of wound infections," *Colloids and Surfaces B: Biointerfaces*, vol. 173, pp. 776–787, 2019.

[6] K. Yang, Q. Han, B. Chen et al., "Antimicrobial hydrogels: promising materials for medical application," *International Journal of Nanomedicine*, vol. Volume 13, pp. 2217–2263, 2018.

[7] B. Gupta, R. Agarwal, and M. S. Alam, "Hydrogels for wound healing applications," in *Biomedical Hydrogels*, S. Rimmer, Ed., pp. 184–227, Woodhead Publishing, 2011.

[8] S. Dhivya, V. V. Padma, and E. Santhini, "Wound dressings – a review," *Biomedicine*, vol. 5, no. 4, pp. 24–28, 2015.

[9] J. M. Grolman, M. Singh, D. J. Mooney, E. Eriksson, and K. Nuutila, "Antibiotic-containing agarose hydrogel for wound and burn care," *Journal of Burn Care & Research*, vol. 40, no. 6, pp. 900–906, 2019.

[10] A. Francesko, P. Petkova, and T. Tzanov, "Hydrogel dressings for advanced wound management," *Current Medicinal Chemistry*, vol. 25, no. 41, pp. 5782–5797, 2018.

[11] P. Kaur, V. S. Gondil, and S. Chhibber, "A novel wound dressing consisting of PVA-SA hybrid hydrogel membrane for topical delivery of bacteriophages and antibiotics," *International Journal of Pharmaceutics*, vol. 572, p. 118779, 2019.

[12] E. Tamahkar, B. Özkahraman, A. K. Süloğlu, N. İdil, and I. Perçin, "A novel multilayer hydrogel wound dressing for antibiotic release," *Journal of Drug Delivery Science and Technology*, vol. 58, p. 101536, 2020.

[13] A. Shahzad, A. Khan, Z. Afzal, M. F. Umer, J. Khan, and G. M. Khan, "Formulation development and characterization of cefazolin nanoparticles-loaded cross-linked films of sodium alginate and pectin as wound dressings," *International Journal of Biological Macromolecules*, vol. 124, pp. 255–269, 2019.

[14] O. Nadtoka, N. Kutsevol, V. Krysa, and B. Krysa, "Hybrid polyacryamide hydrogels: synthesis, properties and prospects of application," *Molecular Crystals and Liquid Crystals*, vol. 672, no. 1, pp. 1–10, 2018.

[15] O. Nadtoka, P. Virych, T. Bezugla et al., *Antibacterial Hybrid Hydrogels Loaded with Nano Silver*, Applied Nanoscience, 2021.

[16] N. Kutsevol, T. Bezugla, M. Bezuglyi, and M. Rawiso, "Branched dextran-graft-polyacrylamide copolymers as perspective materials for nanotechnology," *Macromolecular Symposia*, vol. 317-318, no. 1, pp. 82–90, 2012.

[17] N. Kutsevol and T. Bezugla, "Influence of structural peculiarities of dextran sulphate-g-polyacrylamide on flocculation phenomen," *Ecological Chemistry and Engineering S*, vol. 2, no. 2, pp. 251–256, 2012.

[18] N. V. Kutsevol, T. N. Bezuglaya, and N. Y. Bezuglyi, "Features of the intramolecular structure of branched polymer systems in solution," *Journal of Structural Chemistry*, vol. 55, no. 3, pp. 548–559, 2014.

[19] N. Kutsevol, J. M. Guenet, N. Melnyk, D. Sarazin, and C. Rochas, "Solution properties of dextran-polyacrylamide graft copolymers," *Polymer*, vol. 47, no. 6, pp. 2061–2068, 2006.

[20] N. V. Kutsevol, T. B. Zheltonozhskaya, O. V. Demchenko, L. R. Kunitskaya, and V. G. Syromyatnikov, "Effect of the structure of poly(vinyl alcohol)-graft-polyacrylamide copolymers on their thermooxidative stability," *Polymer Science, Series A*, vol. 46, no. 5, pp. 518–525, 2004.

[21] W. A. Dorsett-Martin, "Rat models of skin wound healing: a review," *Wound Repair and Regeneration*, vol. 12, no. 6, pp. 591–599, 2004.

[22] L. Parnell and S. W. Volk, "The evolution of animal models in wound healing research: 1993-2017," *Advances in Wound Care*, vol. 8, no. 12, pp. 692–702, 2019.